RSC Advances

PAPER

View Article Online
View Journal | View Issue

Cite this: *RSC Adv.*, 2025, **15**, 34609

Performance and mechanisms of waste-based carbon adsorbents in heavy metal removal – an experimental and theoretical approach

Amey Anant Joshi and Gopi Ragupathy *

Access to safe drinking water is increasingly challenged by rising demand, pollution, and climate change, with heavy metal pollutants having emerged as some of the major contributors to today's environmental degradation, intensifying the water crisis. The presence of hazardous metals like chromium, cadmium and lead is a widespread concern in aquatic ecosystems. This study investigates the removal of Pb^{2+}, Cd^{2+}, and Cr^{6+} ions under a set of predetermined conditions using waste-derived carbon adsorbents particularly granular activated carbon (GAC), GAC coated with chitosan (GAC-CS), *Prosopis juliflora* wood-derived biochar (PJBC), and banana stem char (BN char), through a combined experimental and theoretical approach. Characterization techniques (FESEM, FTIR, XRD, Raman, and BET) confirmed porous structures and functional groups responsible for adsorption. In addition, IR studies before and after were conducted to identify the possible mechanisms involved in the removal of these metals before and after adsorption. The removal efficiency was found to be in the order: Pb > Cd > Cr across all adsorbents. BN char consistently exhibited the highest adsorption capacity for all tested metals, with values of 16.50 ± 0.60 mg g^{-1} for Cr^{6+}, 186.16 ± 0.40 mg g^{-1} for Cd^{2+}, and 252.46 ± 0.60 mg g^{-1} for Pb^{2+}, followed in order by PJ biochar, GAC-CS, and GAC. To further understand the adsorption behaviour, Density Functional Theory (DFT) and QTAIM analyses were performed, which confirmed stronger binding of Pb^{2+} compared to Cd^{2+} and Cr^{6+} through charge transfer and orbital overlap. Although comparative studies on carbon-based adsorbents exist, simultaneous use of experimental evaluation and theoretical modelling has been rarely explored.

Received 31st May 2025
Accepted 9th September 2025

DOI: 10.1039/d5ra03863d

rsc.li/rsc-advances

1. Introduction

Environmental pollution, particularly from heavy metals affecting soil and water, is becoming an increasingly serious issue in today's world. Different industrial processes contribute to heavy metal contamination, which negatively impacts the ecosystem.[1] Heavy metal-polluted wastewater inevitably enters the environment, posing significant risks for both public health and biodiversity. Heavy metals, unlike herbicides, insecticides, and other harmful chemicals, cannot be removed from aquatic habitats and instead persist in sediments, slowly re-entering the water over time.[2,3] Because these contaminants persist and build up in living systems, conventional treatments are frequently ineffective, making it essential to develop cleaner and more efficient alternatives.[4] As a result, efficient methods for eliminating metal ions from wastewater are necessary to prevent environmental and ecological harm, as they are toxic at even low levels and tend to accumulate in organisms.[5] Several approaches have been implemented to extract heavy metals from wastewater, including flotation, coagulation–flocculation, precipitation reactions, electrolysis, oxidation methods, ion exchange, membrane technology, adsorption and biosorption.[6,7] Adsorption is a particularly appealing method among these approaches due to its simple operation, economical nature, and high removal efficiency. Additionally, the reversibility of most adsorption processes allows for repeated use of adsorbents *via* suitable regeneration and desorption techniques.[6–8]

Among the commonly employed adsorbents are carbonaceous substances as well as their modified counterparts. Furthermore, a wide spectrum of materials is available, whose applicability is primarily determined by regional factors such as resources and needs.[9] Also, carbon-based adsorbents have been proven highly effective in the elimination of heavy metal ions and their complexes.[10] Their vast surface area, well-structured internal porosity, reactivation of active sites and presence of several functional groups are the main causes of their exceptional sorption capacity.[11] The creation and application of sustainable, eco-friendly, and green materials in a variety of disciplines has received a lot of attention in recent years.[12–14] As a result, the development of methods that are structurally simple, economically practical, and environmentally sustainable is of great importance.[15] In this aspect, advancements in renewable and biodegradable biomass composites have been

Department of Chemistry, School of Advanced Sciences, Vellore Institute of Technology (VIT), Vellore, 632014, Tamil Nadu, India. E-mail: r.gopi@vit.ac.in

explored for the generation of green and sustainable materials.[16] Numerous valuable and intriguing resources have been derived from degradable materials such as wood biomass, agricultural and food waste, industrial byproducts, herbs and other organic sources.[17] As the most widely available renewable resource on Earth, lignocellulosic biomass originates from plant sources, including agricultural and forestry residues, along with dry grasses cultivated as annual or perennial energy crops.[18]

Lignocellulosic biomass obtained from nature functions as a sustainable supply of energy and raw matter. Lignocellulosic biomass predominantly comprises of three principal components: lignin, hemicellulose and cellulose[19,20] in addition to minor non-structural elements including proteins, chlorophylls, ash, waxes, pectin (commonly found in fibres) and tannins (in wood).[21] Among these natural biopolymers, cellulose is the most widely available and renewable on the planet.[22] In general, lignocellulosic biomass contains cellulose in varying proportions, typically between 17% and 77%.[17,19] Lignin is another polymeric substance found in lignocellulosic materials, where its concentration fluctuates between roughly 10% and 30%. Lignin-enriched biomass, produced at a rate of 40–50 million tons annually, is the most abundant renewable carbon source after cellulose worldwide.[23] Cellulose and hemicellulose within biomass are expected to decompose into volatile compounds, while the less reactive lignin fraction contributes to the development of solid char.[24] The higher the lignin content, the greater the char formation, which is linked to lignin's stability at high temperatures and its OCH_3 group composition.[25] As a result, carbon-rich fraction of lignocellulosic biomass, lignin serves as the major contributor to the adsorption process among its three primary components.[17,21] This inherent carbon abundance, together with its molecular diversity, enables the transformation of biomass into carbon materials with tailored structures, thereby making them suitable for a broad spectrum of applications.[26,27]

To achieve this, thermal degradation processes are often employed to transform carbon-rich biomass into functional carbon materials. Thermal degradation of carbonaceous substances through pyrolysis generates char, hydrocarbon liquids, water, light-weight organics, and gaseous emissions. The solid carbonaceous product generated through pyrolysis is known as char.[28] During pyrolysis, thermal decomposition extracts moisture and volatile matter from biomass, resulting in char with unique characteristics compared to its precursor.[24,29] The process facilitates biomass breakdown, increasing its stability, hydrophobic traits and the preliminary development of porosity.[30,31] The most significant changes are observed in surface area, porosity, pore structures and chemical properties, including ash content and elemental composition.[32] Due to these transformations, char exhibits higher reactivity, thereby making it feasible for use as an adsorbent.[33] Consequently, char becomes a beneficial secondary product, commonly utilized in the manufacture of biochar, activated carbons which function as efficient adsorbents for treating wastewater.[27,34]

We identified and selected two different biomass origins: a wood-based species (*Prosopis juliflora*) and a plant-derived feedstock (coconut shell and banana stem). The research focused on the selection of various chars from different biomass feedstocks. This included commercially available granular activated carbon (GAC) derived from coconut shell, biochar obtained from *Prosopis juliflora* (PJ biochar) wood and pyrolyzed product from banana stem (BN char) prepared under partial oxidation conditions. Moreover, chitosan was utilized to coat granular activated carbon (GAC-CS), producing a functionalized adsorbent. These adsorbents were evaluated to assess their peak adsorption capacity for extracting heavy metals, specifically cadmium (Cd), chromium (Cr) and lead (Pb), from synthetic aqueous solutions. Cluster analysis findings suggested that biochars originating from feedstocks of similar nature exhibited comparable traits and were grouped in the same category.[35] Hence this study aims to evaluate various types of chars derived from different feedstocks for the selection of an appropriate adsorbent, providing a basis for feedstock selection based on removal efficiency. Additionally, we performed Density Functional Theory (DFT) analysis to explore the mechanistic pathways influencing the elimination of these toxic metal ions. Using Density Functional Theory, we were able to examine the electronic properties and binding behaviour between metals and possible adsorbents at a quantum mechanical level. This method offered in-depth understanding of the adsorption mechanism, including the evaluation of binding energies and the characterization of the chemical bonds formed during interaction.

2. Materials and methods

2.1 Biomass and different carbon materials

As previously mentioned, various types of carbonaceous materials were obtained from multiple sources. Commercial granular activated carbon (GAC), manufactured from coconut shells and possessing a particle size range of 3–5 mm, was procured from CG Carbon Pvt. Ltd, located in Kerala, India. In addition, *Prosopis juliflora* wood was collected from the premises of Vellore Institute of Technology (VIT). Furthermore, banana stems were obtained from nearby local markets.

2.2 Chemicals and reagents

The chemicals and reagents employed in this investigation were of analytical quality. Low-molecular-weight chitosan was sourced from Sisco Research Laboratories Pvt. Ltd (SRL, India). Potassium dichromate ($K_2Cr_2O_7$) was also obtained from SRL. Cadmium chloride monohydrate ($CdCl_2 \cdot H_2O$) was procured from LOBA Chemie Pvt. Ltd. Lead nitrate (Pb $(NO_3)_2$) and concentrated nitric acid (HNO_3) were acquired from Thermo Fisher Scientific, Qualigens brand (India). Concentrated hydrochloric acid (HCl, AR grade) was supplied by Rankem (Avantor, India).

2.3 Preparation of different carbon materials

2.3.1 Chitosan functionalized coconut shell derived granular activated carbon (GAC-CS). A method reported in the literature by Vinitnantharat *et al.*, with slight modification was employed to synthesize chitosan-coated GAC.[36] Two grams of

chitosan were dissolved in 250 millilitres of a 1% (v/v) acetic acid solution, and the mixture was constantly stirred throughout the night to create a chitosan solution. In an Erlenmeyer flask, 12.5 g of GAC particles were mixed with 250 mL of 1% (w/v) NaOH solution and stirred at 250 rpm for 24 hours. The mixture was filtered to isolate the particles, which were then dried. The particles were then immersed in a chitosan gel solution with a 5 : 1 AC to chitosan ratio and agitated for 24 hours at 250 rpm. Afterward, deionized water was used to rinse the materials until neutrality was achieved, after which they were vacuum-dried in a desiccator.

2.3.2 *Prosopis juliflora* biochar (PJ biochar). The biochar, made from *Prosopis juliflora* wood, was prepared in the biomass power plant at VIT campus and was generously made available for analysis by the CO_2 Research and Green Technologies Centre, VIT. The initial step involved cutting the wood into smaller pieces. The wood was then left to dry under the sun, allowing it to naturally reduce moisture content. After sufficient drying, the wood was then pyrolyzed at 550 °C in the absence of air. The resulting biochar was retrieved after the pyrolysis process and was ground into a fine powder. The fine powder was then thoroughly washed using double-distilled water to remove any residual ashes or impurities. After washing, the material was dried for 24 hours at 105 °C in an oven to eliminate any last traces of moisture.

2.3.3 Banana char (BN char). The banana stem was first cut into small fragments to ensure uniform size, which facilitates effective washing and drying. After that, these parts were cleaned with double-distilled water to get rid of contaminants like dust and dirt. To get rid of any remaining moisture, the pieces were cleaned and then dried for 24 hours at 105 °C in an oven. Following the drying process, the material was ground into a fine powder and passed through a 150-micron mesh sieve. The sieved powder was pyrolyzed by heating in a muffle furnace at 400 °C for 3 hours in an open crucible (without a lid) to ensure proper thermal decomposition. The heating rate was maintained at 12 °C per minute.

3. Batch adsorption experiments

Adsorption experiments were carried out at room temperature, approximately 23 ± 1 °C. For the preparation of stock solutions (1000 ppm) of Pb^{2+}, Cr^{6+}, and Cd^{2+}, Pb $(NO_3)_2$, $K_2Cr_2O_7$, and $CdCl_2 \cdot H_2O$ were dissolved in deionized water, respectively. The intended working solutions of 50, 100 and 200 ppm were made by diluting the stock solutions. To perform the batch experiments, 25.00 mg of adsorbent was added in a 100 mL Erlenmeyer flask, and then heavy metal aqueous solutions (50 mL) were added. A total of six solutions containing 50 ppm of chromium, cadmium, and lead were prepared. Then the flasks were shaken for a maximum of three hours at 180 rpm while placed on the orbital shaker. At intervals of 30 minutes, the solution was withdrawn, filtered using filter paper, and the concentration of heavy metals remaining in the supernatant was assessed *via* Atomic Absorption Spectroscopy (AAS). The following equation was employed to determine the adsorption capacity of the adsorbents:

$$q_e = \frac{(C_0 - C_e) \times V}{m}$$

where, q_e (mg g^{-1}) is the amount of heavy metal adsorbed at equilibrium per gram of adsorbent; V (L) is the volume of the solution; C_0 and C_e (ppm) refer to the initial and equilibrium concentrations of the heavy metal in solution, respectively; and m (g) corresponds to the mass of the dry adsorbent used.[37]

4. Results and discussion

4.1 Characterisation

A detailed investigation employing multiple characterisation techniques was conducted to examine the surface composition and morphology of the prepared materials. FTIR spectroscopy was utilized to detect the functional groups, whereas Raman analysis was carried out to assess the graphitic structure of the material. The crystallographic structure of the samples was examined through XRD analysis. Furthermore, SEM and FESEM analyses were also conducted to visualize the surface characteristics of the samples, while the BET method was utilized to quantify pore dimensions, specific surface area and total pore volume.

4.1.1 FTIR analysis. The FTIR spectrum of *Prosopis juliflora* wood biochar exhibited a distinct peak at 3428 cm^{-1}, which is characteristic of hydroxyl groups commonly associated with alcohols.[38] Peaks were also seen at 2922 cm^{-1} and 2852 cm^{-1} which suggesting the symmetric C–H bond and C–H stretching vibrations, confirming the presence of methyl and methylene groups typically found in carbohydrates.[39] Additionally, an spectral band at 1629 cm^{-1} indicated C–O carbonyl stretching, shows the presence of acetyl moieties in hemicellulose and the aldehyde group in lignin.[40] Peaks at 1429 cm^{-1} were attributed to carbon–carbon stretching vibrations within aromatic rings,[41] whereas the C–O stretching vibrations in the HO–C=O and –C=O groups were linked to the bands at 1115 cm^{-1} and 1062 cm^{-1}, respectively.[42]

A noticeable spectral band at 3439 cm^{-1} was found in the BN char FTIR spectra, shows the presence of hydroxyl (–OH) groups typical of alcohols.[43] The adsorption bands at 2854 cm^{-1} and 2925 cm^{-1} were consistent with C–H stretching vibration in aliphatic hydrocarbons, suggesting the contribution of methyl and methylene groups from carbohydrate residues.[44] An absorption band around 1745 cm^{-1} suggested the presence of unconjugated C=O groups, typically found in aliphatic carboxylic acids or ketone derivatives produced from hemicellulose.[45] The carbonyl groups in conjugation were identified by a distinctive peak at 1635 cm^{-1}, which typically arises from lignin and the C=C stretching vibration of an aromatic ring.[37,46] Similarly, C=C stretching vibrations in aromatic rings were linked to peaks between 1400 and 1500 cm^{-1}, whereas C–O–C, O–C–C, and C–O–H stretching vibrations from carbohydrates, including cellulose and lignin, were found close to 1034 cm^{-1}.[47,48]

For the analysis of the IR spectrum, the GAC samples were finely ground into powder and mixed with potassium bromide (KBr) to form pellets suitable for measurement. The spectrum exhibited a strong and broad peak within the range of 3300–

3600 cm^{-1}, because of the O–H stretching vibrations of alcohol groups.[49] Absorption peaks appearing at 2922 cm^{-1} and 2851 cm^{-1} corresponded to C–H stretching vibrations in aliphatic saturated groups, commonly found in hydrocarbons.[50] An adsorption band at 1745 cm^{-1} can be linked to the vibrational stretching of C=O bonds found in functional groups such as lactones, carboxylic acids, esters and anhydrides.[51] The FTIR spectrum also exhibited distinct bands at 1630 cm^{-1} and 1120 cm^{-1}, associated with carbonyl and phenolic functionalities within the sample.[52] Additionally, peak at 1571 cm^{-1} was identified, primarily associated with the C=C bonds in benzene rings. The IR spectrum of GAC coated with chitosan demonstrated slight shifts in peak positions compared to uncoated GAC, confirming the successful coating of chitosan on the GAC surface (Fig. 1).

4.1.2 XRD analysis. The X-ray Diffraction (XRD) analysis of PJ biochar revealed different peaks corresponding to cellulose type I, part of the α-cellulose crystallographic family, identified at 2θ angles of 23.15°, 36.10°, and 39.55°.[41] Furthermore, peaks at 2θ angles of 23.15°, 24.97°, 29.48°, and 43.27°, matching well with the standard reference JCPDS no. 81-0792.[39] The detection of a broadened peak at 25° can be accounted to the amorphous nature of carbon present in the material.[40] Additionally, a peak at 2θ = 43.0° likely represents organic polymers or crystallite present in the original biomass.The XRD pattern of BN char exhibited a prominent peak at 2θ = 28.54°, corresponding to disordered graphite, characteristic of a turbostratic carbon structure.[53] In addition, the appearance of peaks at 29.52° and 40.50° confirms the presence of thermally altered kaolinite.[54] Likewise, the minor diffraction peaks at 2θ = 50.25°, 66.45°, and 73.73° can be linked to the development of calcite structures.[54] In the XRD analysis of GAC, two broad peaks observed in the 2θ ranges of 20–30° and 40–50° confirm the amorphous structure of the material, attributed to the disordered stacking of carbon ring systems.[55] Each sample's XRD pattern features two broad reflections at 24.48° and 43.63°, indicative of the (002) and (100) planes of graphite, as documented in JCPDS card no. 00-056-0159.[56] A diffraction peak appeared at 24.48°, associated with carbonaceous structures originating from coconut shell biomass and commonly observed in pyrolyzed biochars rich in lignin or cellulose.[57,58] In the case of GAC-CS, slight deviations in the diffraction peaks shown the existence of a chitosan coating on the GAC surface. The resulting changes in the graphitic structure confirmed successful incorporation and a corresponding transformation in crystal order.

4.1.3 Raman spectroscopy. The structural ordering and disorder of carbon in GAC and GAC-CS samples were

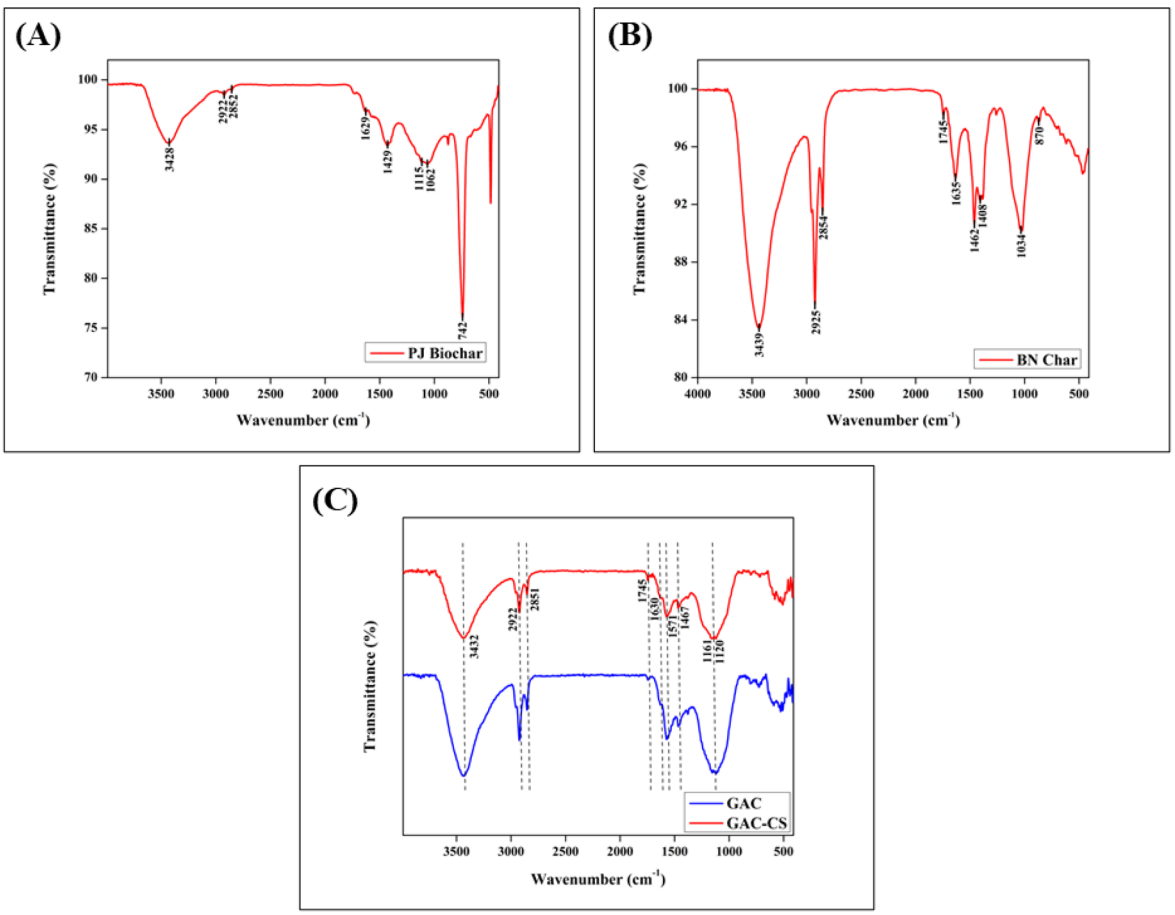

Fig. 1 FTIR spectra of (A) – PJ biochar (B) – BN char (C) – GAC and GAC-CS illustrating the surface functional groups present in the material.

investigated using Raman spectroscopy, which shed light on the various structural forms of carbon. According to the Raman examination, both samples had two distinctive carbon material peaks, known as the G and D-bands. These reflect the presence of crystalline graphite and structural imperfections, respectively.[59] The stretching vibrations of the sp^2-bonded pairs are associated with the G-band, indicating complete graphitisation of the GAC. Conversely, the D-band represents the presence of sp^3 defects, serving as an indicator of structural disorder in the carbon material's structure.[57,60] The D and G band, which are indicative of GAC's structural characteristics, can be clearly seen at 1342 cm^{-1} and 1583 cm^{-1}, respectively. These bands do, however, show a modest shift towards lower wavenumbers following the chitosan coating (GAC-CS), showing up at 1314 cm^{-1} and 1576 cm^{-1} for the D and G band, respectively. This modification indicates that the chitosan layer has altered the surface chemistry or structural arrangement. Moreover, the reduced intensity of these bands in GAC-CS further supports the successful deposition of chitosan on the surface of GAC (Fig. 2).

4.1.4 SEM and FE-SEM analysis. The morphological features of the synthesised chars were analysed through SEM and FESEM techniques, and the corresponding images are provided in Fig. 3. These images reveal the development of porous networks and the extent of surface roughness, which are both affected by the pyrolysis conditions and the type of input materials. The elemental makeup of the samples was also determined by using Energy Dispersive X-ray Spectroscopy (EDX) as a characterisation method. The corresponding EDX (S3) spectra as well as additional microscopic images of SEM a(S1) and FE-SEM (S2) analysis are presented in the SI. At 500× magnification, the SEM micrograph of PJ biochar reveals a surface morphology characterized by smooth ridges and sharply defined edges. As magnification increases, PJ biochar reveals a network of interconnected pores of different diameters in the FESEM images, highlighting its heterogeneous porous structure. At a higher magnification level (5000×), the micrograph highlights unevenly distributed pores of different sizes and mostly oval or circular shapes, giving the surface a honeycomb-like appearance. The porous structure formed as a result of the efficient thermal degradation and volatilization of organic matter, mainly hemicellulose and cellulose, between 200–400 °C, as observed in SEM images from studies carried out at a carbonization temperature of 550 °C.[61,62]

The SEM micrograph of BN char reveals that it possesses a fragmented and porous texture, characterized by irregular particle shapes and a distribution of pores with varying sizes across the surface. Similarly, FE-SEM images reveal well-defined pore channels and a fragmented char structure. The surface irregularities indicate non-uniform pore distribution, characterized by a richly textured and porous network with numerous interconnected voids. Higher-resolution images reveal a surface characterized by crack formations and thin, flake-like sheets.

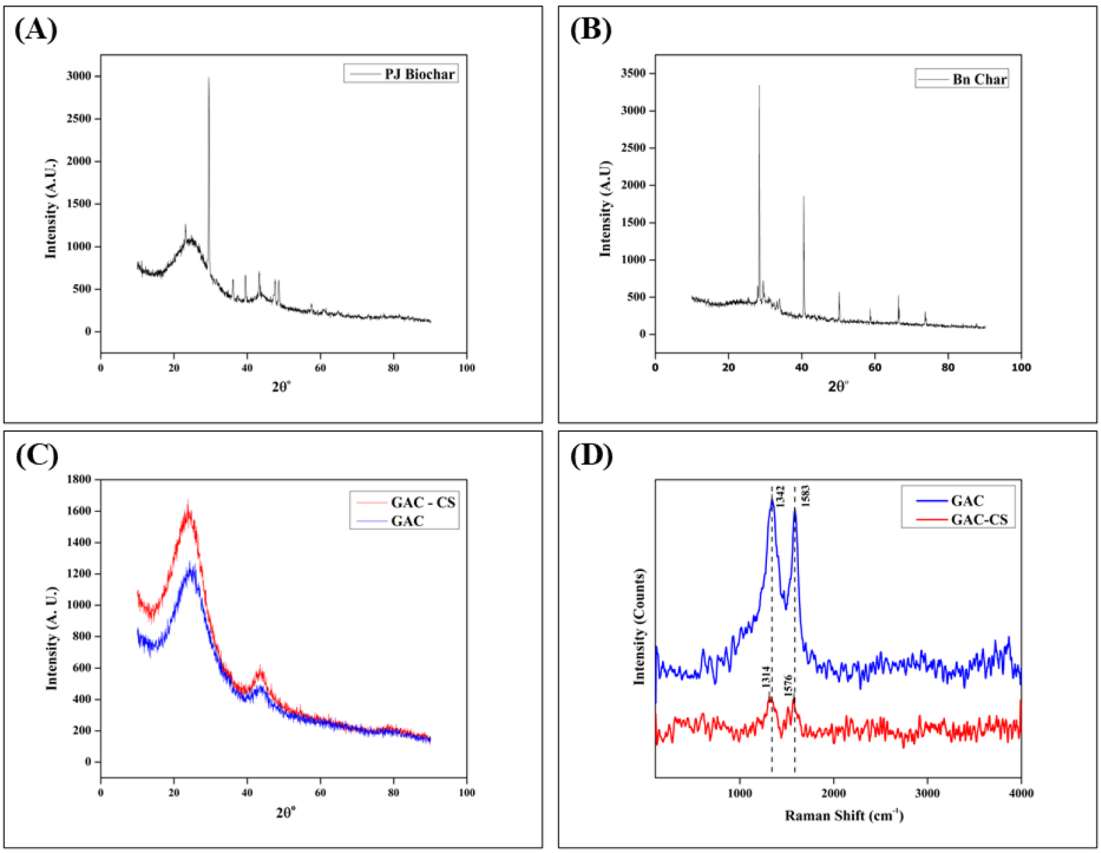

Fig. 2 XRD patterns of (A) – PJ biochar (B) – BN char (C) – GAC and GAC-CS and Raman spectra of (D) GAC and GAC-CS.

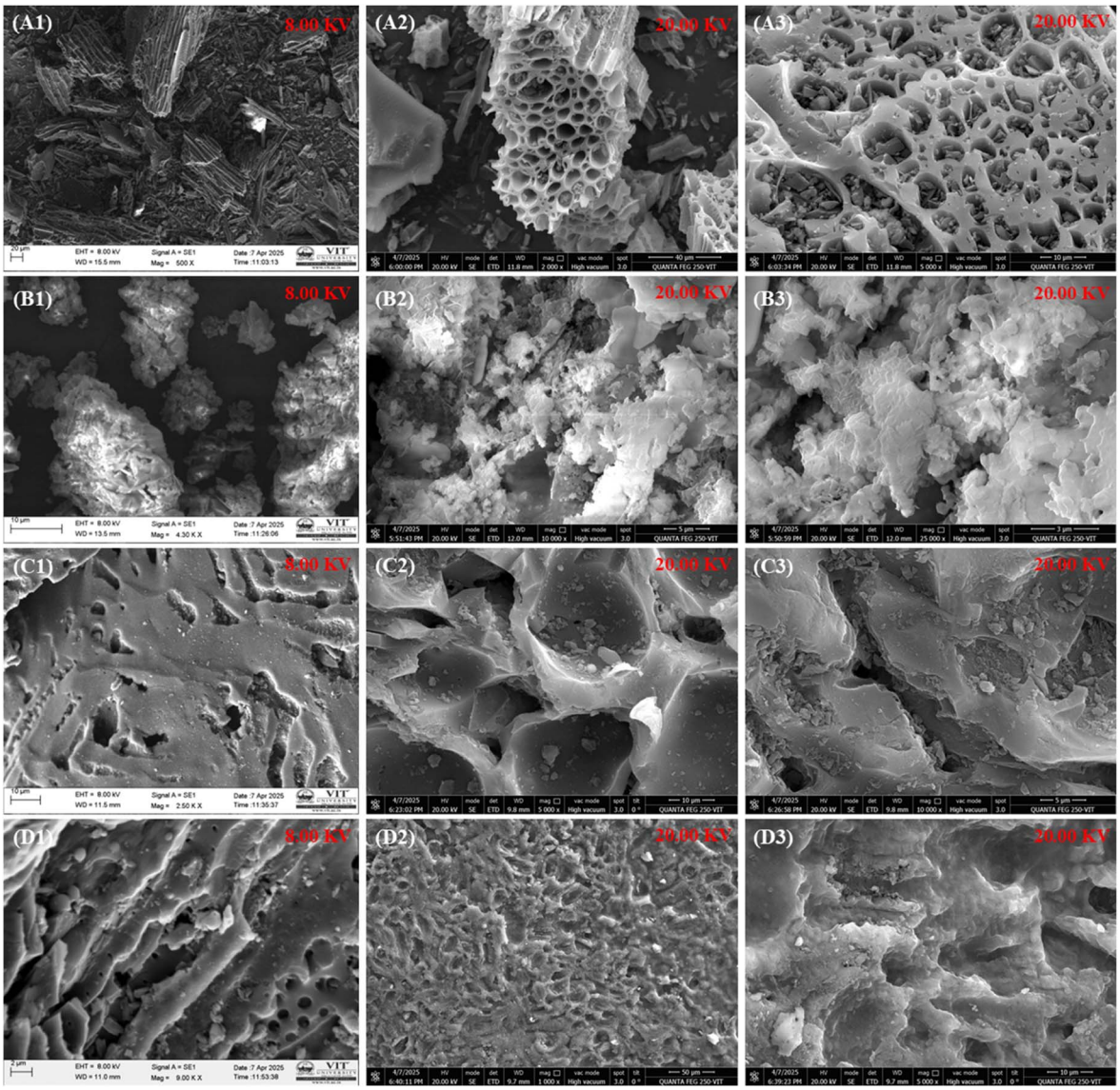

Fig. 3 SEM images (A1, B1, C1, D1) and FE-SEM images (A2, A3, B2, B3, C2, C3, D2, D3) of (A) PJBC, (B) BN char, (C) GAC, and (D) GAC-CS, respectively, showing surface morphology.

This layered structure suggests exfoliation as a result of thermal treatment, while the cavities between the layers indicate the release of gases during carbonization. The surface of GAC, as observed under SEM, reveals a porous framework containing open and irregularly shaped pores and voids with pores scattered across its surface. The material also displays several sharply defined fractures and surface cracks. Under magnification, the FESEM image depicts a surface marked by exfoliated sheet formations and an extensive porous network. The presence of multiple fractures and voids is noticeable, with increased visibility of interlayer cracks. Similar to GAC, the SEM micrograph of GAC-CS exhibits a porous texture with multiple irregularly formed pores of various sizes. Upon careful examination, the high-resolution FESEM images clearly demonstrate the application of a coating layer on the surface of GAC, confirming that chitosan has been successfully applied and adhered to the material. The presence of this uniform coating layer not only confirms the successful deposition of chitosan but also suggests strong adhesion to the carbon substrate.

4.1.5 BET surface area analysis. Using nitrogen adsorption–desorption testing, the BET analysis was carried out to examine the surface characteristics of the char samples, with an emphasis on surface area, pore volume, and pore size distribution. Additionally, the BJH (Barrett–Joyner–Halenda) method was employed to further assess the pore size distribution from the adsorption isotherm. The BET adsorption–desorption isotherms and pore size distribution graphs for GAC and GAC-CS are shown in Fig. 4, with (A) and (B) representing GAC, GAC-CS whereas (C) and (D) representing BN char and PJ biochar, respectively. The microporous structure of GAC and GAC-CS is indicated by their adsorption behaviour, which is consistent with the Type I isotherm model, which is frequently linked to

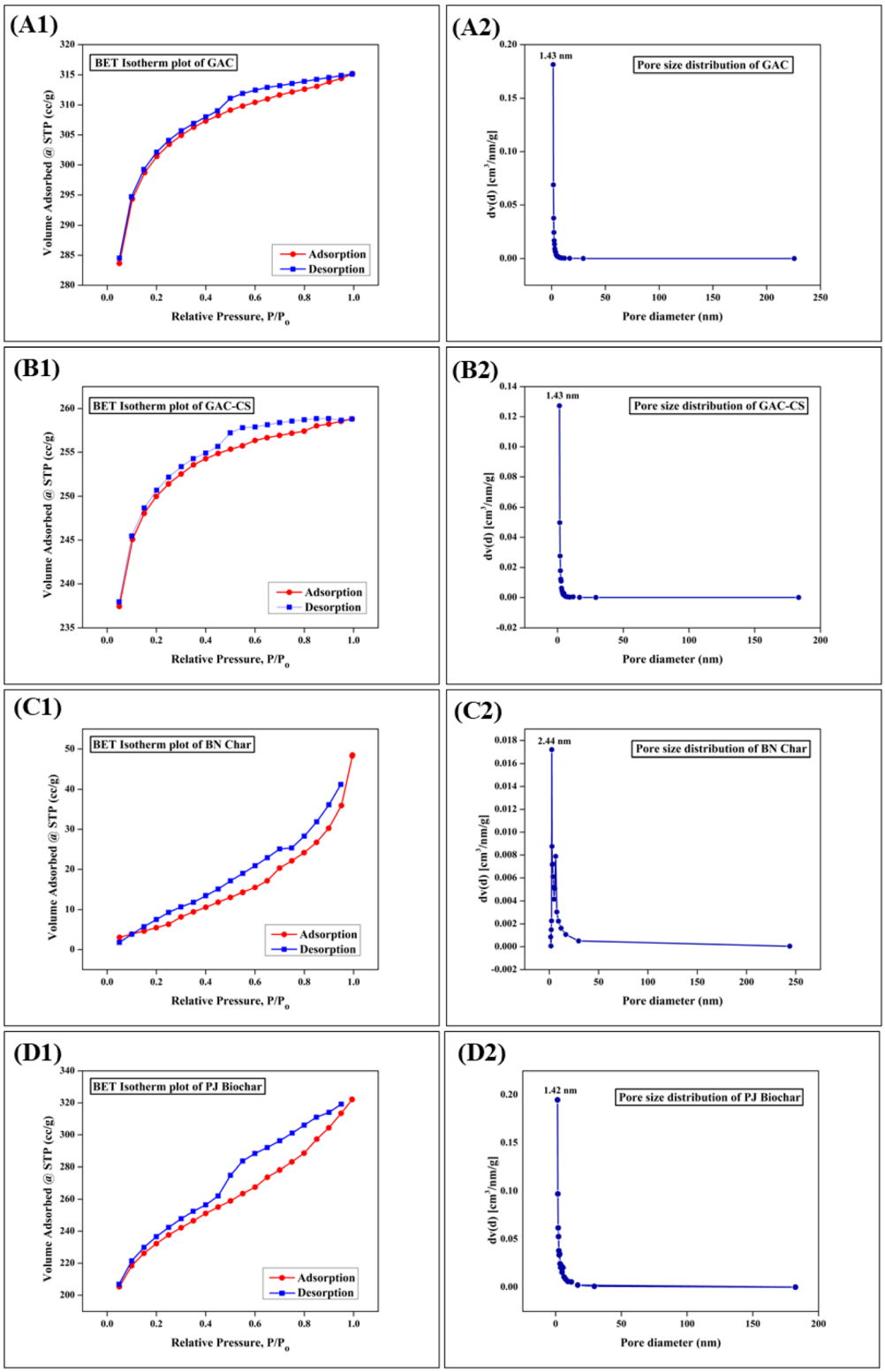

Fig. 4 Image representing BET adsorption–disorption isotherm of (A1) GAC, (B1) GAC-CS, (C1) BN char, (D1) PJ biochar and pore size distribution of (A2) GAC, (B2) GAC-CS, (C2) BN char, (D2) PJ biochar.

microporous materials. The pore size of 1.43 nm, which lies in the standard microporous range of 1–2 nm, further confirms the microporous nature of GAC and GAC-CS.

The BET results indicate that the surface area of GAC (1137.817 $m^2 g^{-1}$) was significantly greater than that of GAC-CS (942.169 $m^2 g^{-1}$). Furthermore, a reduction in pore volume was

observed after chitosan coating on GAC, decreasing from 0.110 $cm^3\ g^{-1}$ to 0.078 $cm^3\ g^{-1}$, despite the pore diameter remaining unchanged at 1.42 nm. Thus, a reduction in BET surface area without alteration in pore size implies that the chitosan layer may have partially blocked the pores and reduced the available surface. The BET analysis of BN char revealed a specific surface area of 62.385 $m^2\ g^{-1}$, with a pore volume of 0.084 $cm^3\ g^{-1}$ and pore diameter of 2.44 nm. The nitrogen sorption isotherm of BN char, shown in Fig. 4(C1), has a prominent hysteresis loop and a typical Type IV profile, which is indicative of mesoporous materials according to IUPAC. The loop shape suggests an H3-type hysteresis, evidenced by the progressive uptake on the adsorption side and the rapid desorption transition occurring in the 0.4–0.5 P/P_o range.[63] According to the BET analysis, PJ biochar's specific surface area was 876.678 $m^2\ g^{-1}$, its mean pore diameter was 1.424 nm, and its total pore capacity was 0.286 $cm^3\ g^{-1}$. As illustrated in Fig. 4(D1), the nitrogen adsorption isotherm of PJ biochar exhibits a noticeable hysteresis loop, characteristic of a Type IV profile, much like BN char. Although the mean pore diameter indicates a primarily microporous structure (less than 2 nm), the Type IV hysteresis likely arises from super micropores, a few mesopores, or interconnected networks that induce capillary condensation, a phenomenon commonly observed in biochars and other carbonaceous materials.

4.2 Experimental results

We investigated the adsorption capacity of several carbon-based compounds under predetermined set of conditions in this work. An Erlenmeyer flask (100 mL) holding 50 mL of an aqueous heavy metal solution was filled with precisely 25.00 mg of the chosen adsorbent, which had been previously weighed. This dosage was adopted in accordance with common literature protocols, where 25 mg in 50 mL or similar proportions are frequently used. It facilitates comparability and representativeness, while also balancing measurable removal performance with the precision needed for accurate q_e estimation.[64,65] Six distinct sample solutions with various heavy metal concentrations were created for the investigation. The flasks were then placed on an orbital shaker set at a constant speed of 180 rpm to ensure uniform mixing and facilitate interaction between the adsorbent and the heavy metal ions. Since the standard shaking speed for heavy metal adsorption studies usually falls between 150 and 200 rpm, we adopted 180 rpm as a reasonable midpoint. At 30-minute intervals, solutions were carefully withdrawn, filtered to remove suspended particles, and analysed using Atomic Absorption Spectroscopy (AAS). Each adsorption experiment was performed in triplicate, and the reported values correspond to the mean ± standard deviation, in accordance with standard practices reported in the literature. The 0–180 minutes contact time was selected to capture both the fast initial sorption and the slower progression toward equilibrium, a trend frequently noted for Pb^{2+}, Cd^{2+}, and Cr^{6+} on carbonaceous materials. Literature indicates that equilibrium is generally reached within this period.[66]

4.2.1 Chromium. Under carefully monitored circumstances, the chromium analysis was conducted at 23 ± 1 °C. A 1000 ppm stock solution was precisely diluted to create a 50-ppm chromium solution. 0.1 M hydrochloric acid was used to bring the pH of the solution down to 4.1 ± 0.1. The pH was maintained at 4.1, as mildly acidic conditions have consistently been reported to enhance Cr(VI) uptake on carbon-based adsorbents.[67–69] Concentrated hydrochloric acid was diluted to the appropriate molarity to create the 0.1 M HCl solution. The above-mentioned procedure was then carried out with various adsorbents, including GAC, GAC-CS, PJ biochar and BN char by adding 25 mg of each adsorbent to the respective solutions. After the adsorption process, the final concentration of chromium in the solutions was determined using Atomic Absorption Spectroscopy (AAS).

An investigation into chromium removal using granular activated carbon (GAC) and chitosan-modified GAC (GAC-CS) showed a decrease in chromium concentration from an initial 50 ppm to 45.30 ± 0.10 ppm and 44.52 ± 0.20 ppm, respectively. This corresponds to chromium removal amounts of 4.70 ppm for GAC and 5.48 ppm for GAC-CS, highlighting their effectiveness in eliminating chromium from aqueous solutions. Similarly, chromium removal using BN char resulted in a decrease of 8.25 ppm of chromium from the initial concentration. In comparison, PJ biochar showed a slightly lower removal, decreasing the chromium concentration by 6.32 ppm. These results suggest that BN char exhibited a higher adsorption capacity for chromium. The analysis reveals that the adsorption capacity of BN char is 16.50 ± 60 mg g^{-1}, which is higher compared to the other carbon materials, such as PJ biochar (12.64 ± 40 mg g^{-1}), GAC-CS (10.96 ± 40 mg g^{-1}), and GAC (9.40 ± 20 mg g^{-1}). This indicates that BN char has greater efficiency in adsorbing chromium from the solution compared to the other carbon sources. In terms of chromium removal efficiency, BN char outperformed all other materials, achieving 16.50 ± 60%, while PJ biochar, GAC-CS, and GAC reached 12.64 ± 40%, 10.96 ± 40%, and 9.49.40 ± 20%, respectively (Fig. 5).

4.2.2 Cadmium. A 1000 ppm stock solution was precisely diluted to provide 50 ppm and 100 ppm cadmium solutions for the cadmium analysis. No pH adjustment was made before using this solution. However, a measurement of the solution's pH revealed that it was roughly 6.0 ± 1. Different adsorbents were added to the cadmium solution using the same method as for the chromium study in order to evaluate how well they removed cadmium ions. After the adsorption process, the final cadmium concentration in the solution was measured, allowing for the calculation of the adsorption capacity of each adsorbent.

The analysis of cadmium removal using granular activated carbon (GAC) and chitosan-modified GAC (GAC-CS) revealed a decline in cadmium concentration from an initial 50 ppm to 33.75 ± 0.30 ppm and 31.85 ± 0.30 ppm, respectively. Treatment of cadmium-contaminated water using PJ biochar derived from *Prosopis juliflora* resulted in a greater removal of cadmium concentration, reaching a final value of 27.62 ± 0.30 ppm from the original 50 ppm. This corresponds to an adsorption capacity of 44.76 ± 0.60 mg g^{-1}, indicating a moderately effective

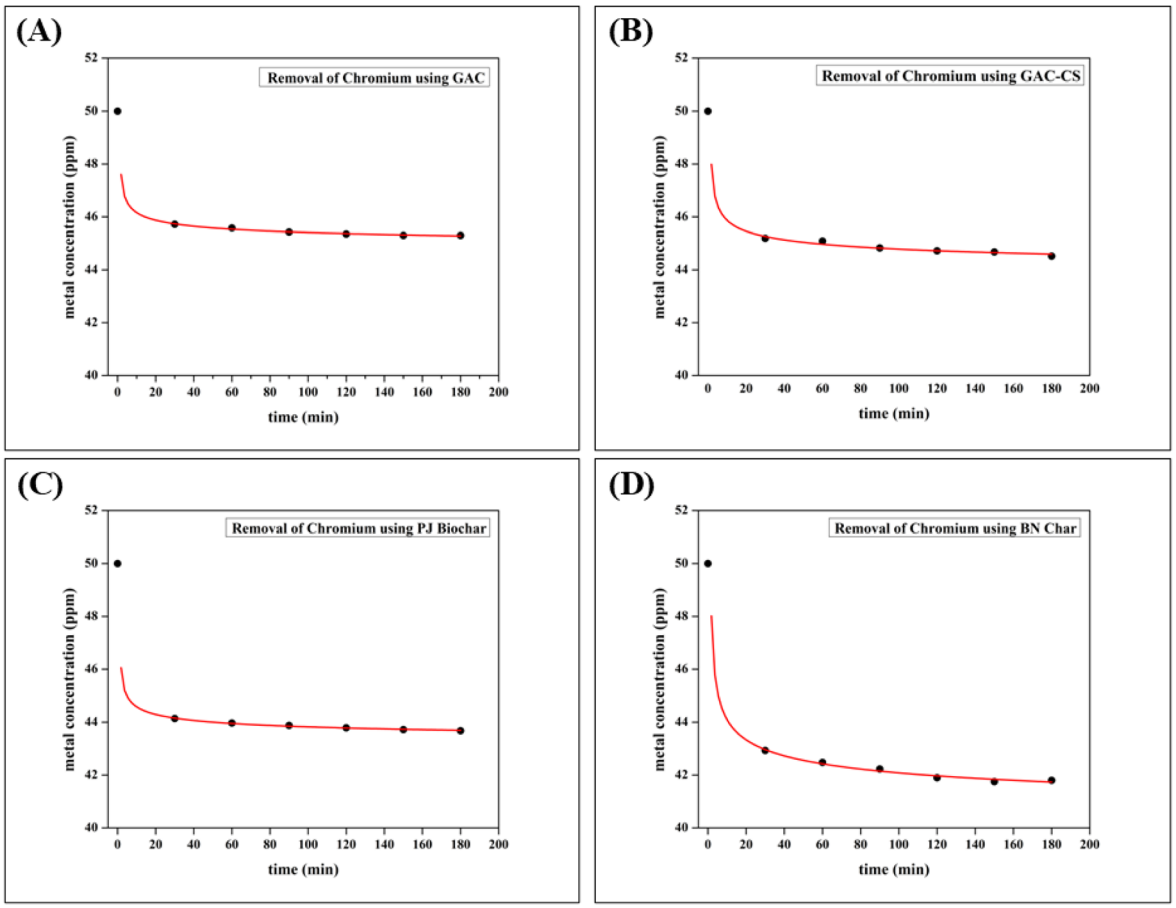

Fig. 5 Graphs of the removal of chromium with (A) – GAC (B) – GAC-CS (C) – PJ biochar (D) – BN char.

removal performance. In contrast, BN char demonstrated the highest performance, removing the cadmium concentration from an initial 100 ppm to 6.92 ± 0.20 ppm, achieving a substantial adsorption capacity of 186.16 ± 40 mg g^{-1}. The comparative analysis of adsorption capacities shows clear differences among the tested adsorbents. GAC and GAC-CS exhibited capacities of 32.5 ± 0.60 mg g^{-1} and 36.30 ± 0.60 mg g^{-1}, respectively, suggesting that the inclusion of chitosan marginally improved cadmium uptake. PJ biochar showed the capacity of 44.76 ± 0.60 mg g^{-1}, while BN char's capacity of 186.16 ± 40 mg g^{-1} greatly outperformed the others. In terms of removal efficiency, BN char is the most effective material, with a removal efficiency of 93.08 ± 40%. PJ biochar followed with 44.76 ± 0.60%, while GAC-CS and GAC showed lower efficiencies of 36.30 ± 0.60% and 32.5 ± 0.60%, respectively (Fig. 6).

4.2.3 Lead. A 1000 ppm stock solution was accurately diluted to prepare 50, 100 and 200 ppm lead solutions for analysis. The pH of the solution was not adjusted before use; however, it was measured and found to be approximately 5.0 ± 1. Various adsorbents were introduced to the lead solution following the same procedure used in the chromium adsorption study. The amount of lead that remained in the solution after the adsorption process was determined. These measurements were used to calculate the adsorption capacity of each material adsorbent, providing insight into their performance in lead removal. The use of granular activated carbon (GAC) led to a decrease in lead concentration from 50 ppm to 25.40 ± 0.20 ppm, while its chitosan-modified counterpart (GAC-CS) brought the concentration down slightly further to 24.16 ± 0.20 ppm. Banana char (BN char), when applied to a solution initially containing 200 ppm of lead, achieved a substantial decrease in concentration to 73.77 ± 0.30 ppm. Similarly, *Prosopis juliflora* wood char (PJ biochar) proved to be highly effective, reducing lead levels from 100 ppm to 3.53 ± 0.40 ppm. In terms of adsorption capacity, banana char stood out with a higher value of 252.46 ± 0.60 mg g^{-1}, indicating its excellent capability to bind lead ions. PJ biochar also demonstrated strong adsorption with a capacity of 192.94 ± 0.80 mg g^{-1}. In contrast, both GAC and GAC-CS displayed lower capacities of 49.20 ± 0.40 mg g^{-1} and 51.68 ± 0.40 mg g^{-1}, respectively. When comparing removal efficiencies, banana char demonstrated 63.12 ± 0.60% removal, while PJ biochar showed a higher efficiency of 96.47 ± 0.80%. However, it should be noted that the initial concentration for PJ biochar (100 ppm) was considerably lower than that used for banana char (200 ppm). GAC-CS showed a slightly better removal efficiency (51.68 ± 0.40%) than unmodified GAC (49.20 ± 0.40%) (Fig. 7) (Table 1) (Fig. 8).

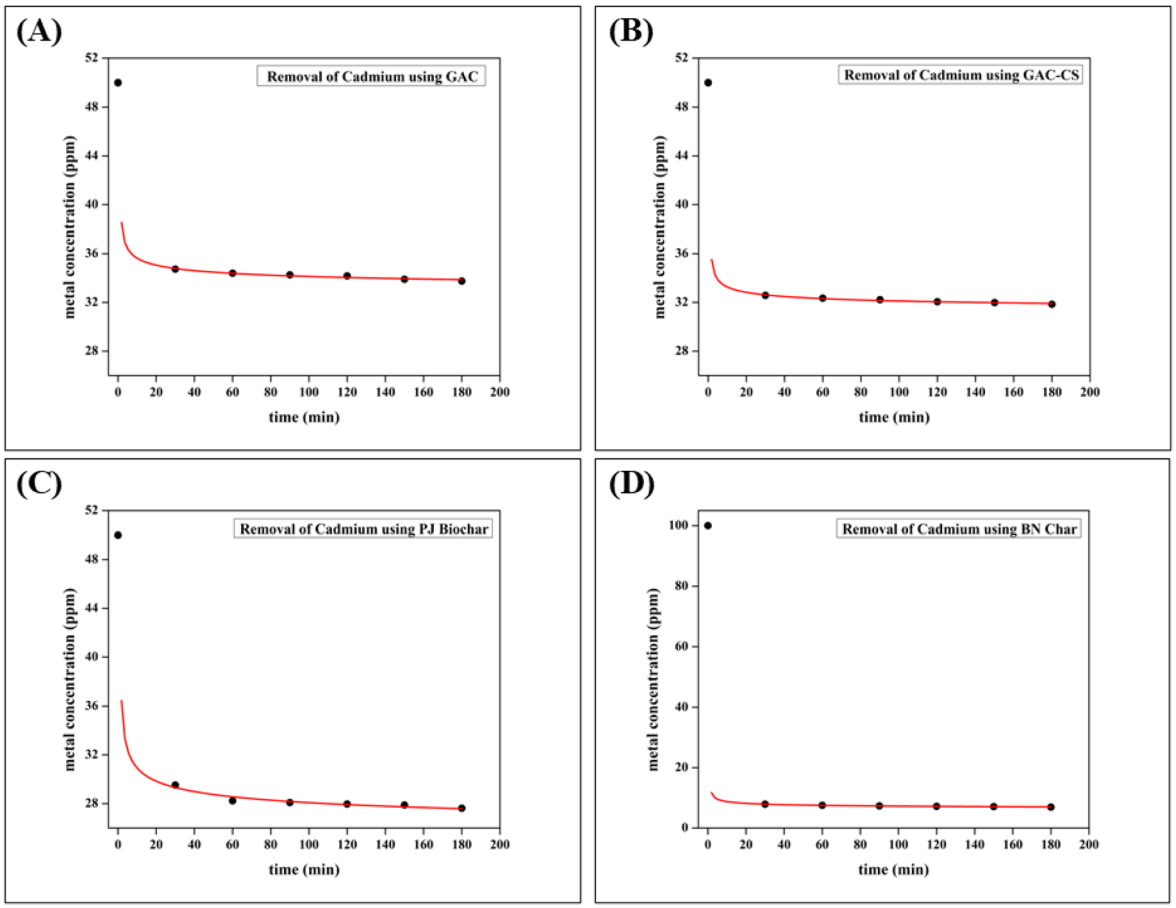

Fig. 6 Graphs of removal of cadmium with (A) – GAC (B) – GAC-CS (C) – PJ biochar (D) – BN char.

Table 1 Adsorption performance of different adsorbents for chromium, cadmium, and lead

Experiment	Adsorbent	Initial conc. (ppm)	Final conc. (ppm)	Removal eff. (%)	Capacity (mg g^{-1})
Chromium	GAC	50	45.30 ± 0.10	9.40 ± 20	9.40 ± 20
	GAC-CS	50	44.52 ± 0.20	10.96 ± 40	10.96 ± 40
	PJ biochar	50	43.68 ± 0.20	12.64 ± 40	12.64 ± 40
	BN char	50	41.75 ± 0.30	16.50 ± 60	16.50 ± 60
Cadmium	GAC	50	33.75 ± 0.30	32.5 ± 0.60	32.5 ± 0.60
	GAC-CS	50	31.85 ± 0.30	36.30 ± 0.60	36.30 ± 0.60
	PJ biochar	50	27.62 ± 0.30	44.76 ± 0.60	44.76 ± 0.60
	BN char	100	6.92 ± 0.20	93.08 ± 40	186.16 ± 40
Lead	GAC	50	25.40 ± 0.20	49.20 ± 0.40	49.20 ± 0.40
	GAC-CS	50	24.16 ± 0.20	51.68 ± 0.40	51.68 ± 0.40
	PJ biochar	100	3.53 ± 0.40	96.47 ± 0.80	192.94 ± 0.80
	BN char	200	73.77 ± 0.30	63.12 ± 0.60	252.46 ± 0.60

4.3 Discussion

The adsorption experiments conducted in this study provide a comparative evaluation of the performance of selected carbon-based adsorbents in removing heavy metals from aqueous solutions. From the experimental adsorption studies, it is evident that the adsorptive capacities of the tested materials follow the order: BN char > PJ biochar > GAC-CS > GAC. This trend clearly demonstrates the superior performance of banana char in sequestering metal ions from aqueous solutions. In terms of metal-specific behaviour, Pb^{2+} ions were found to be adsorbed most effectively across all adsorbents, whereas Cd^{2+} showed comparatively lower uptake, and Cr^{6+} exhibited the least affinity. This indicates that the adsorption process is strongly influenced not only by the surface characteristics of the adsorbents but also by the intrinsic properties of the metal ions, such as ionic radius, hydration energy, and preferred binding interactions.

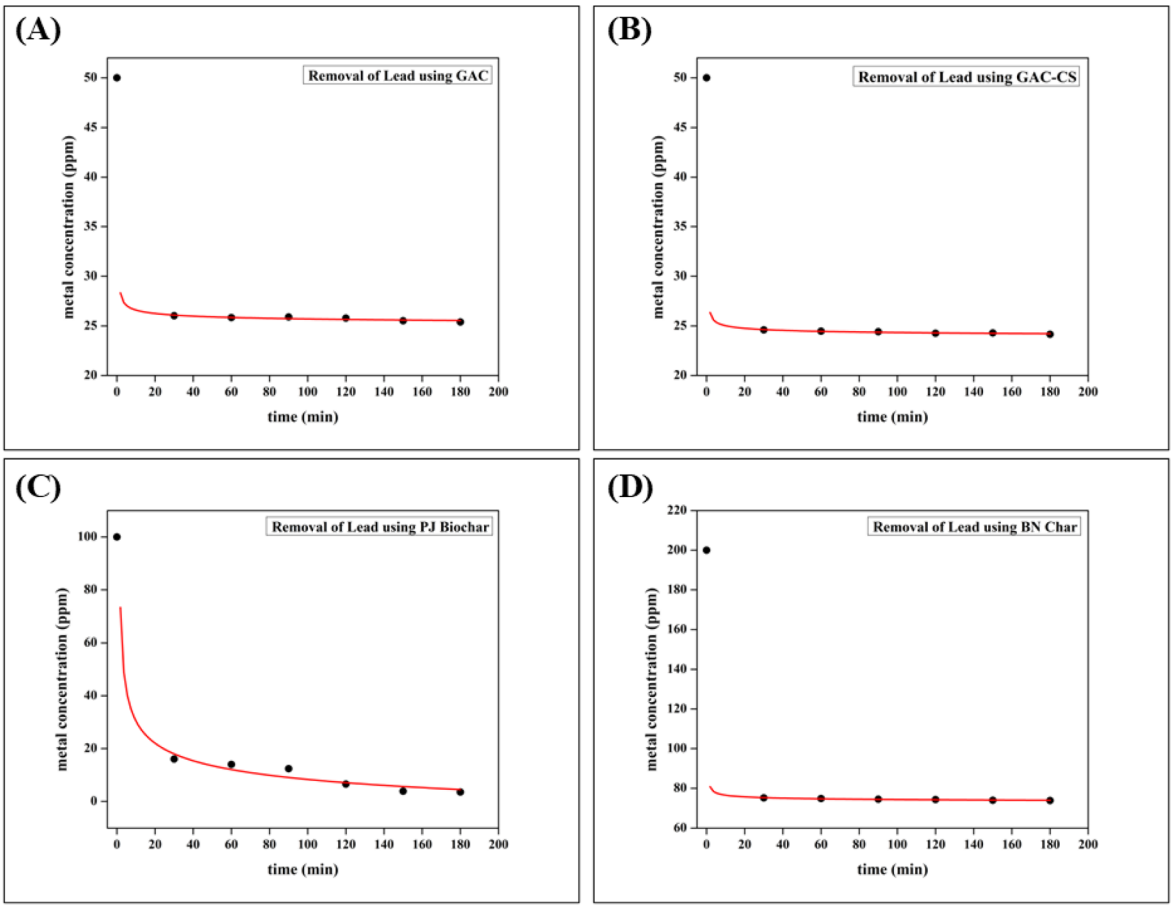

Fig. 7 Graphs of lead removal from solution using (A) – GAC (B) – GAC-CS (C) – PJ biochar (D) – BN char.

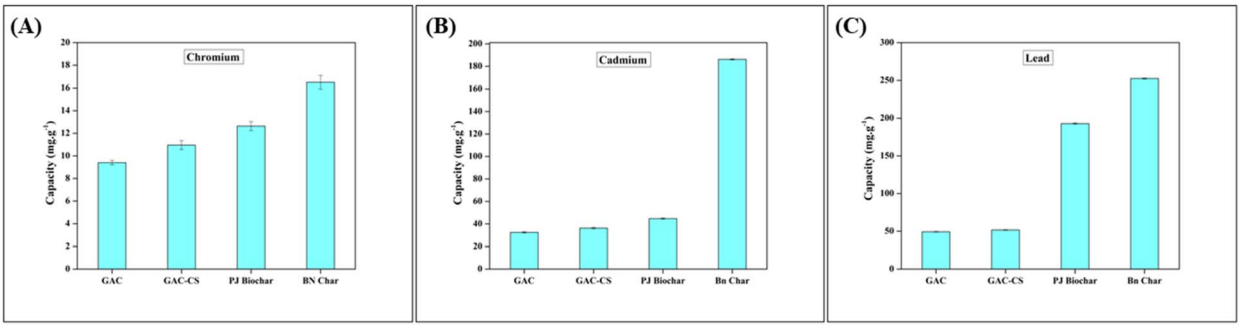

Fig. 8 Adsorption capacities of different adsorbents for (A) chromium, (B) cadmium, and (C) lead ions. Error bars indicate standard deviation.

The analysis of metal removal using granular activated carbon (GAC) and its chitosan-modified form (GAC-CS) revealed that the adsorption performance of the two materials did not differ significantly. Across all metals tested, the uptake capacities of GAC and GAC-CS remained comparable, suggesting that the chitosan coating imparted only a marginal, if any, improvement in adsorption efficiency. The chitosan coating introduces extra functional groups, including amine ($-NH_2$) groups, onto the GAC surface, potentially improving its chromium adsorption capacity. Raman analysis showed modest shifts in the D and G bands along with decreased band intensities, suggesting alterations in the structural order of the carbon framework. Complementary SEM and FESEM observations confirmed these results by revealing the presence of a coating layer on the GAC surface. However, it was observed that the modification with chitosan did not lead to an appreciable improvement in chromium removal. This may be attributed to the dual effect of chitosan, which introduces functional groups that can facilitate metal adsorption while simultaneously causing partial blockage of pores on the GAC surface. BET surface area analysis further supported this observation, showing a decrease in specific surface area from

1137.82 $m^2 g^{-1}$ for GAC to 942.17 $m^2 g^{-1}$ for GAC-CS. The reduction was accompanied by a decline in pore volume from 0.110 to 0.078 $cm^3 g^{-1}$, whereas the average pore diameter remained nearly unchanged (~1.42 nm), suggesting pore blockage rather than structural collapse. As a consequence, the effective accessibility of the adsorbent's porous network is reduced, which in turn limits the overall adsorption capacity, as the diffusion of metal ions into the pores of GAC-CS becomes restricted. This structural limitation helps to explain why the adsorption performance of GAC-CS did not differ significantly from that of unmodified GAC, despite the introduction of additional functional groups through chitosan coating.

In overall comparison, banana char exhibited superior adsorption capacity compared to the other tested adsorbents. The observed variations in adsorption efficiency could be attributed to differences in the surface properties, porosity, and functional groups of the materials, influencing their ability to capture metal ions from the solution. Although BN char exhibited a remarkably low BET surface area (62.4 $m^2 g^{-1}$) compared to other adsorbents GAC (1137.8 $m^2 g^{-1}$), GAC-CS (942.169 $m^2 g^{-1}$) and PJ biochar (876.678 $m^2 g^{-1}$), its adsorption capacity for all the tested metals was significantly higher. This unexpected outcome can be understood by analysing variations in pore distribution and surface functionalities. BET analysis revealed that other adsorbents possess a predominantly microporous structure (~1.42–1.43 nm), which may restrict the diffusion of hydrated metal ions and thereby limit the effective utilization of its high surface area. In contrast, BN char exhibited a mesoporous framework with an average pore size of ~2.44 nm and a pronounced H3-type hysteresis loop, indicative of slit-shaped pores that enhance ion accessibility. Complementary FTIR analysis showed comparatively stronger band intensities for BN char, particularly in regions associated with O–H, C=O, and C–O vibrations, suggesting a higher abundance of oxygen-containing functional groups that act as strong binding sites for metal ions through electrostatic attraction, ion exchange, and complexation. Furthermore, SEM observations revealed a layered, sheet-like morphology in BN char, which provides abundant edge sites and interlayer voids that facilitate rapid ion diffusion and effective interaction with functional groups. When considered together, the presence of accessible mesopores, the abundance of oxygenated functional groups and the layered morphology account for the superior metal adsorption of BN char as compared to other selected adsorbents, even with its relatively low BET surface area. On the other hand, PJ biochar, despite exhibiting a higher surface area, contained fewer surface functional groups, as evidenced by the lower FTIR band intensities associated with oxygen-containing moieties. This reduction in functionalities can be attributed to its higher pyrolysis temperature (550 °C), at which many oxygenated groups are thermally degraded, in contrast to BN char prepared at 400 °C. Consequently, the lower density of active binding sites likely contributed to the inferior adsorption performance of PJ biochar as compared to BN char.

4.4 Interpretation of removal mechanism through FT-IR study

Carbon-rich substances obtained from waste are primarily composed of lignin, hemicellulose and cellulose. Owing to the abundance of functional groups in these components, FT-IR spectroscopy can be applied to study their interaction with heavy metal ions. The IR spectra of adsorbents were expected to alter following metal ion adsorption due to the coordination of functional groups with metal ions. Fig. 9 presents a comparison of IR spectra of different adsorbents after adsorption with all three metals.

Similar peaks observed in the FT-IR spectra of BN char and PJ biochar suggest that their surfaces possess functionally similar groups. The FT-IR spectra of both adsorbents reveal a broad peak at 3000–3500 cm^{-1}, which could be linked to carboxylic and hydroxyl groups, with absorption likely caused by the stretching of free or H-bonded OH^- groups. The interaction between the metals and the functionalities on the adsorbent's surface is further supported by a decrease in the strength of these peaks. Similarly, the observed peaks at 1748 cm^{-1} in BN char and 1733 cm^{-1} in PJ biochar, attributed to C=O stretching, decrease in intensity upon metal adsorption, implying potential metal interactions. The C=O and C=C stretching vibrations of aromatic rings, originating from lignin, appear in the 1400–1500 cm^{-1} range and show reduced intensity after adsorption, suggesting interactions with metal ions. Furthermore, the high-intensity bands in the 1034–1364 cm^{-1} range, can be linked to C–O stretching vibrations from cellulose, lignin, and hemicellulose, exhibit decreased intensity following metal adsorption. A comparison of the original spectrum before adsorption reveals that C–O peaks were significantly stronger and broader than C=O groups before adsorption, indicating that C–O functional groups are more prominent on the adsorbent surface. Similarly, a decrease in peak intensity is seen for glycosidic bonds in cellulose and C–H bending vibrations, indicating structural modifications.

An in-depth examination of the FT-IR spectra for BN char and PJ biochar following adsorption of lead, chromium, and cadmium metal reveals that lead causes the greatest decline in peak intensity, signifying strong adsorption onto functional groups. In contrast, chromium displays minimal peak intensity reduction, except in the 1350–1500 cm^{-1} range, where an opposite trend is noticed. This suggests that lead interacts with more diverse functional groups with stronger interaction at the adsorbent surface whereas chromium's binding is more selective and limited. Similarly, upon comparing the spectra of all three adsorbents before and after metal adsorption for each individual metal, it is evident that BN char exhibits the most significant decline in peak intensity for all three metals compared to its pre-adsorption spectra, suggesting superior adsorption capacity. PJ biochar, however, exhibits the least variation in peak intensity, indicating weaker metal adsorption. These results demonstrate that BN char is more effective among both the adsorbents for removing heavy metals.

The FT-IR spectra of these chars suggest that they contain different functional groups such as carboxyl (–COOH) and

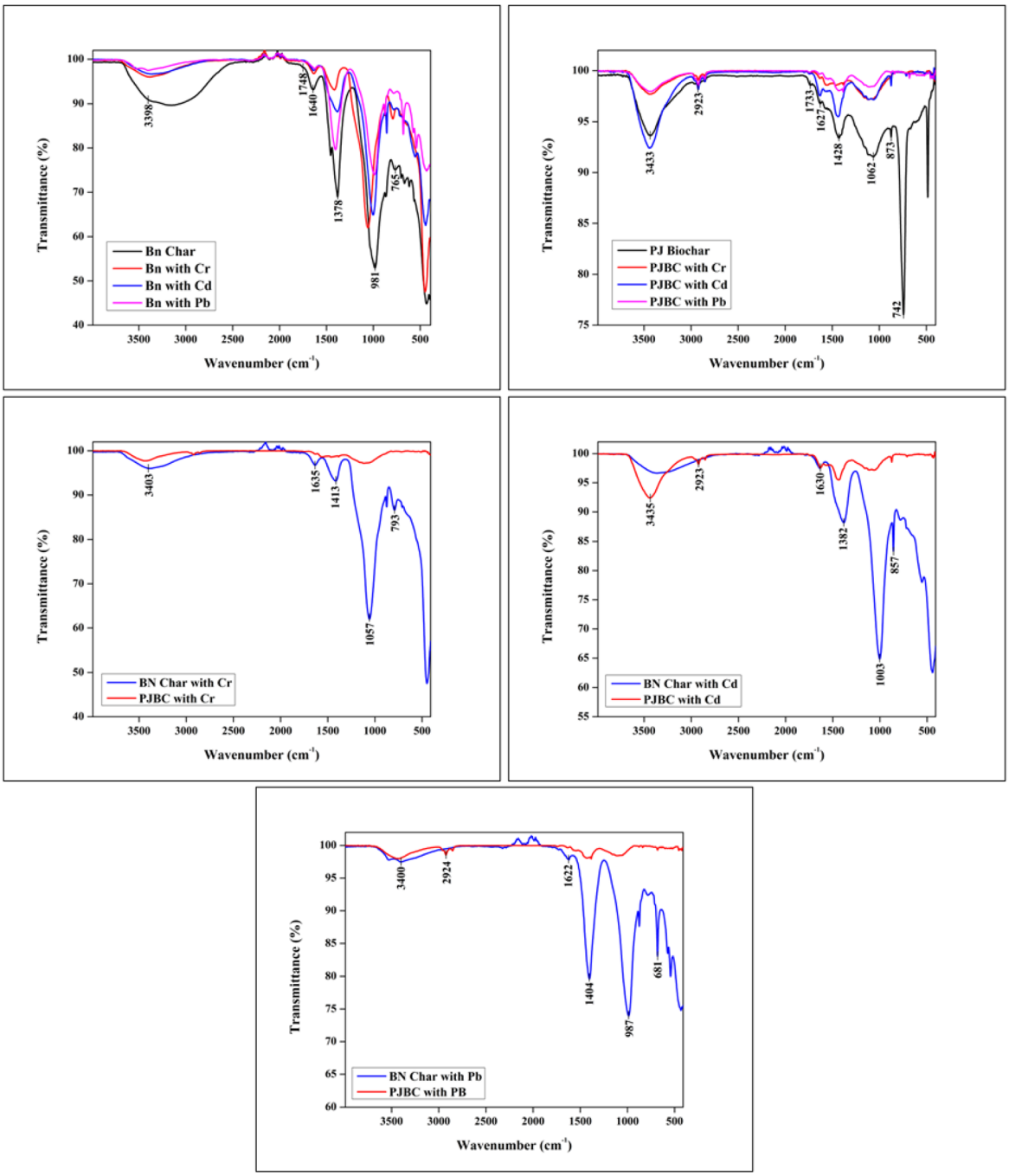

Fig. 9 Comparison of IR spectra of all adsorbents with chromium, cadmium and lead.

hydroxyl (–OH) groups, which enhance their potential to bind with metal ions. The weakening of these peaks implies that metal adsorption occurred *via* functional group interaction. Positive heavy metal ions interact with negatively charged carbon adsorbents through electrostatic forces, particularly when functional groups are present to facilitate the interaction. Therefore, adsorption may take place *via* an electrostatic mechanism, initiated by the attraction between positively charged metals and negatively charged adsorbent sites. It is also feasible for protons and heavy metals on oxygen-rich functionalities, like carboxyl and hydroxyl groups, to exchange ions, suggesting that ion exchange may be one of the methods for removing heavy metals. Analysis of the IR spectra of adsorbents before and after metal adsorption, displays peak shifts in the carboxyl functional group region. This observation indicates that metal complexation with carboxyl groups is one of the pathways in the adsorption process. Also, being primarily composed of lignin, cellulose, and hemicellulose, these adsorbents contain phenolic and lactonic groups. Thus, one of the main pathways for heavy metal removal is surface

complexation, in which metal ions form stable associations with the functional groups present on the adsorbent surface, resulting in their efficient uptake from solution. Based on the IR analysis, it can be concluded that metal adsorption is facilitated by pore filling physical adsorption, alongside ion exchange, electrostatic interactions and surface complexation with functional groups like carboxylic, hydroxyl, lactonic and phenolic groups present on the adsorbent surface.

5. Computational study

In the past few years, theoretical analysis has been utilized alongside experimental techniques to enhance the understanding of adsorption.[70] These theoretical calculations yield significant insights into structural properties, energy states and electronic density maps at the atomic level.[71] The molecular models were developed using Gauss View, and their interactions were examined through Gaussian 16 software.[72] The interaction of metals with a system containing fused benzene rings and saturated carbon atoms, resembling the Graphite like surface with multiple functional groups, was investigated using DFT calculations. Earlier scientific findings have indicated that these structures are characteristic of carbon-based materials.[73] Several theoretical research on transition metals supports the use of the B3LYP hybrid functional as an efficient method for predicting structural arrangements and energy profiles. Consequently, the chosen compounds were optimised using the 6-31G(d) basis set in conjunction with the B3LYP theoretical technique.[74] To perform DFT calculations involving metal atoms, the extensively used LANL2DZ basis set was chosen for Cd^{2+}, Pb^{2+}, and Cr^{6+} ions.[75] The output data from DFT calculations were processed and visualized through GaussView 6.0 software to analyse molecular structures.[76] The coordinates of the selected structures are provided in SI (Section S6).

Fused benzene rings were used to simulate carbonaceous surfaces, resembling a graphite (111)-like configuration and saturated carbon atoms.[77] In order to examine the role of functional groups in metal adsorption on carbonaceous materials, various nitrogen and oxygen based functional groups, including carboxyl, hydroxyl, methoxy and amine, were incorporated into the carbon surface (Fig. 10). DFT calculations were used to analyse the interaction of metals with the simulated molecular structure. Molecular electrostatic potential (MEP), interaction energy, thermodynamic variables, frontier molecular orbitals (FMO) and structural parameters were studied, whereas topological properties were examined using the quantum theory of atoms in molecules (QTAIM). To calculate the binding energy (ΔE_{bind}) of the metals on the carbonaceous surface, the following equation was used:

$$\Delta E_{bind} = E_{complex} - [E_{metal} + E_{surface}] \quad (1)$$

where, $E_{complex}$ is the total energy associated with the metal-carbonaceous surface complex, E_{metal} is the energy associated with metal ion, and $E_{surface}$ is the energy associated with the carbonaceous surface.[77] Furthermore, the formulas provided in equations were used to determine the thermodynamic variables, specifically enthalpy (ΔH) and Gibbs free energy (ΔG). Eqn (2) and (3).[78]

$$\Delta H = H_{complex} - [H_{metal} + H_{surface}] \quad (2)$$

$$\Delta G = G_{complex} - [G_{metal} + G_{surface}] \quad (3)$$

Numerous reactivity indices, including chemical hardness (η), electronegativity (χ), chemical softness (S), chemical potential (μ), electrophilicity index (ω) and nucleophilicity index (N), were computed using the HOMO and LUMO energy values. These parameters were determined using eqn (4)–(9), in accordance with density functional theory (DFT) and Koopmans' theorem.[79]

$$\text{Electronegativity}(\chi) = \frac{IP + EA}{2} \quad (4)$$

$$\text{Chemical hardness}(\eta) = \frac{IP - EA}{2} \quad (5)$$

$$\text{Chemical softness}(S) = \frac{1}{2\eta} \quad (6)$$

$$\text{Chemical potential}(\mu) = -\frac{(IP + EA)}{2} \quad (7)$$

$$\text{Electrophilicity index}(\omega) = \frac{\mu^2}{2\eta} \quad (8)$$

$$\text{Nucleophilicity index}(N) = \frac{1}{\omega} \quad (9)$$

QTAIM (Quantum Theory of Atoms in Molecules) investigations were performed to examine the fundamental nature of the interactions between heavy metal ions and adsorption surfaces. By analysing electron density distribution, QTAIM allows for a deeper understanding of how atoms interact within chemical bonds.[79,80] The analysis involved examining kinetic energy ($G(r)$), potential energy ($V(r)$), electron density ($\rho(r)$) and Laplacian of electron density ($\nabla^2\rho(r)$). Additionally, the total electronic energy ($H(r)$) at the Bond Critical Point (BCP) was derived through eqn (10).[80,81] Furthermore, the FT-IR spectra for all complexes were computed and are included in the SI (S10).

$$H(r) = G(r) + V(r) \quad (10)$$

5.1 Molecular electrostatic potential (MEP) analysis

The role of MEP is significant in assessing electron cloud distribution and recognizing nucleophilic and electrophilic regions within a molecule. The reactivity of a molecule can be assessed through MEP mapping, where intense red coloration signifies regions of greater negative electrostatic potential, whereas blue areas indicate higher positive potential.[78] The MEPs of the optimized structures, depicted in Fig. 11, indicate that hydrogen-abundant regions display blue coloration, signifying a higher electrostatic potential that is likely to attract nucleophiles. On the other hand, electronegative atoms such as

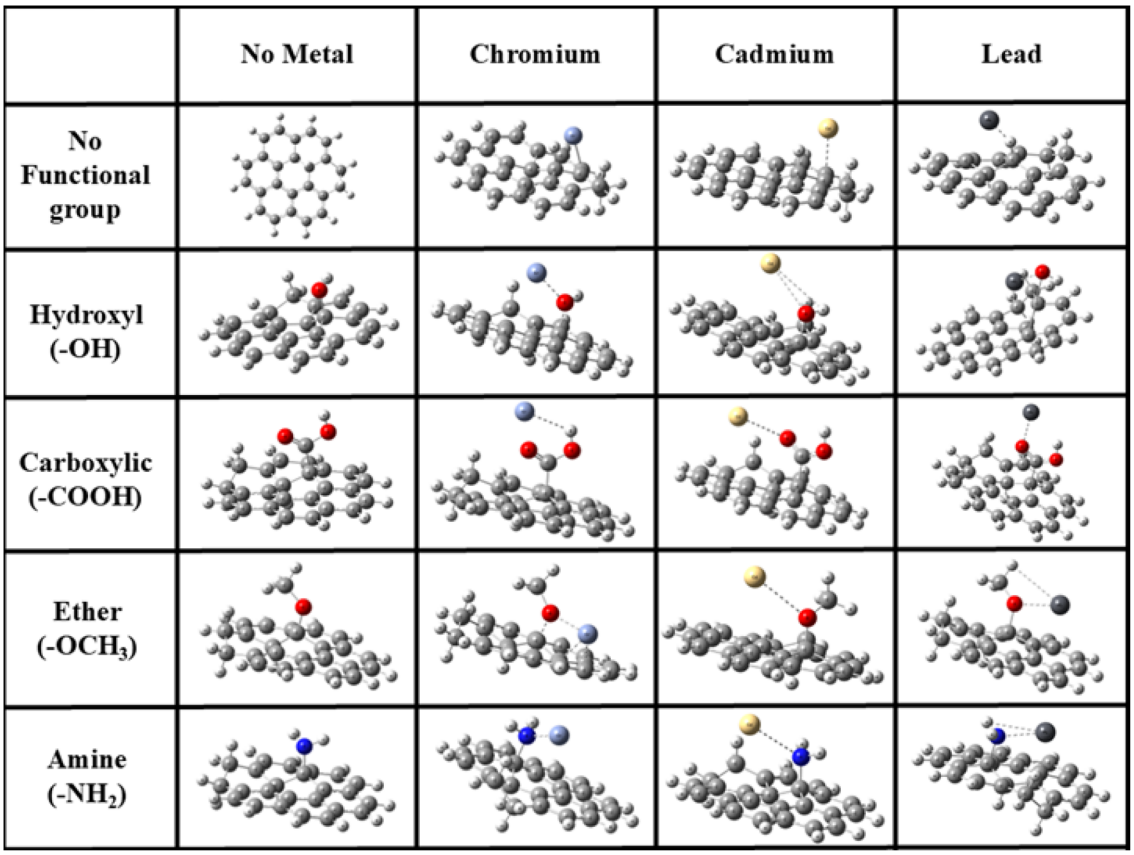

Fig. 10 Optimized structures of a graphite-like surface and its complexes with Cr, Cd, and Pb, computed using the 6-31G(d) basis set and the B3LYP functional.

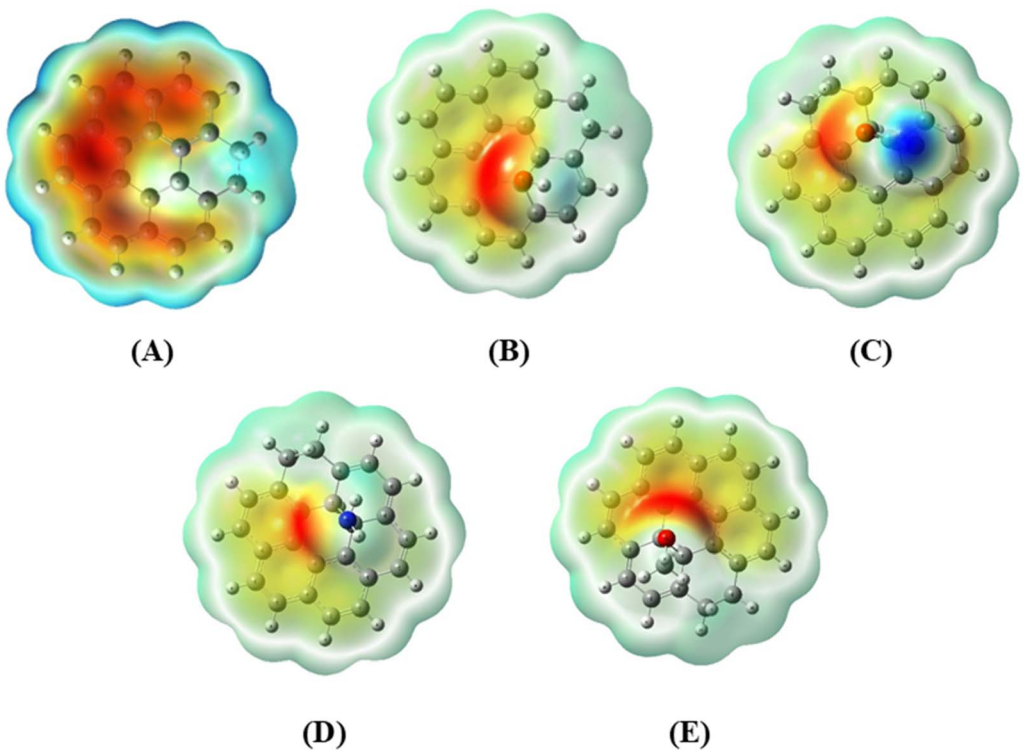

Fig. 11 Molecular electrostatic potential of (A) graphite (111) like plane (B) graphite with –OH functionality (C) graphite plane with –COOH moiety (D) graphite plane with $-OCH_3$ functional group (E) graphite plane with $-NH_2$ group.

oxygen and carbon contribute to red coloured areas, representing nucleophilic sites that tend to draw electrophiles. Due to their electropositive nature, metals are expected to form interactions at the red coloured regions of the molecular surface. A detailed visualization of the molecular electrostatic potentials (MEPs) illustrating the interactions of Cr, Cd, and Pb metals with the respective surfaces is provided in SI Section S8.

5.2 Frontier molecular orbital (FMO) analysis

To better comprehend the complexation sites and interactions between Pb^{2+}, Cd^{2+}, and Cr^{6+} with carbonaceous matrices, a frontier molecular orbital analysis was also conducted. The introduction of functional groups onto graphite surfaces leads to a reduction in HOMO energy, with G + OH (−5.39 eV) having the lowest value, while G + COOH (−5.28 eV) remains slightly more electron-donating. Since the HOMO energy of graphite (−5.18 eV) is lower than Cr and Pb but higher than Cd, Cd should theoretically exhibit the strongest adsorption due to its high electron-accepting capability, whereas Pb should show minimal interaction with these surfaces. However, experimental data reveal that Pb exhibits the strongest adsorption on carbon-based materials, suggesting that adsorption is not solely determined by HOMO energy but is also influenced by other factors. Of all the elements, cadmium showed the highest band gap at 5.283 eV, while lead had the lowest at 0.676 eV, indicating its lower stability and greater tendency for chemical interactions. This increased reactivity of Pb presumably allows for greater interactions with carbon-based surfaces. In conclusion, both HOMO energy and the electronic band gap may contribute to metal adsorption behaviour.

The investigation of HOMO–LUMO band structure in graphite like configurations also helps to elucidate the adsorption mechanisms and electronic features of Cd, Cr, and Pb on both pure and functionalized graphite (111) surface. Graphite, in its pure form, possesses a band gap of 3.18 eV, which exhibits negligible alteration after functionalization with NH_2, OH, COOH, and OCH_3, spanning between 3.15 and 3.22 eV. Among these, graphite functionalized with COOH (3.15 eV) exhibits the smallest band gap, signifying improved charge transfer, whereas graphite with OCH_3 (3.22 eV) has the largest, implying minimal electronic alteration. The adsorption of metals on graphite alters its band gap, indicating the degree of interaction. Overall, a lower band gap corresponds to stronger charge transfer and chemisorption, while a higher band gap indicates weaker physisorption interactions. The existence of HOMO and LUMO densities on both the adsorbent and the adsorbate is indicative of a chemisorption mechanism. However, when these densities remain confined to a single entity, the interaction is classified as physisorption.[82] The visualization of HOMO and LUMO orbitals for all metal ions, along with their respective optimized structures, is provided in Fig. 12.

The HOMO–LUMO distribution of Cd, Cr, and Pb with functionalized graphene reveals key aspects of their adsorption behaviour (Fig. 13). It is evident from the figure that for all three metals, the carboxyl (–COOH) and amino ($–NH_2$) functional groups induce a significant localization of HOMO and LUMO densities around the metal-functional group region, resulting in enhanced chemisorption. In Cr-based systems, both –OH and $–NH_2$ groups reveal significant LUMO delocalization across the Cr atom and the surrounding graphite like surface, suggesting strong chemisorptive interactions due to efficient

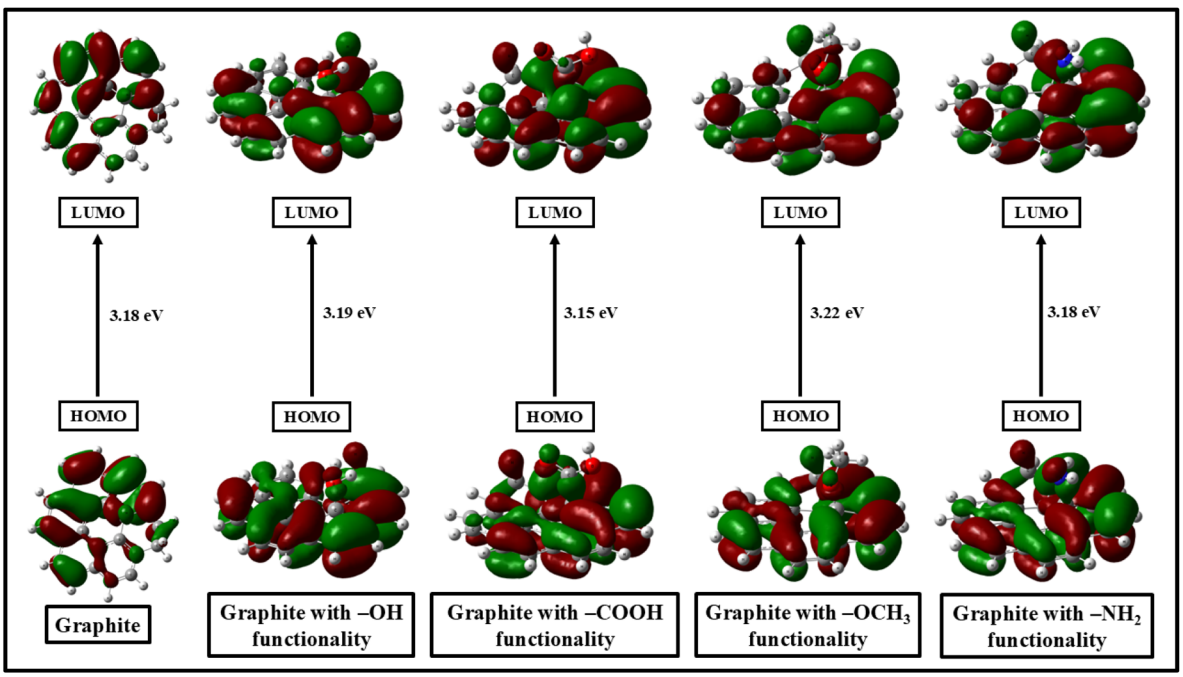

Fig. 12 Image representing the HOMO–LUMO band gap of selected structures.

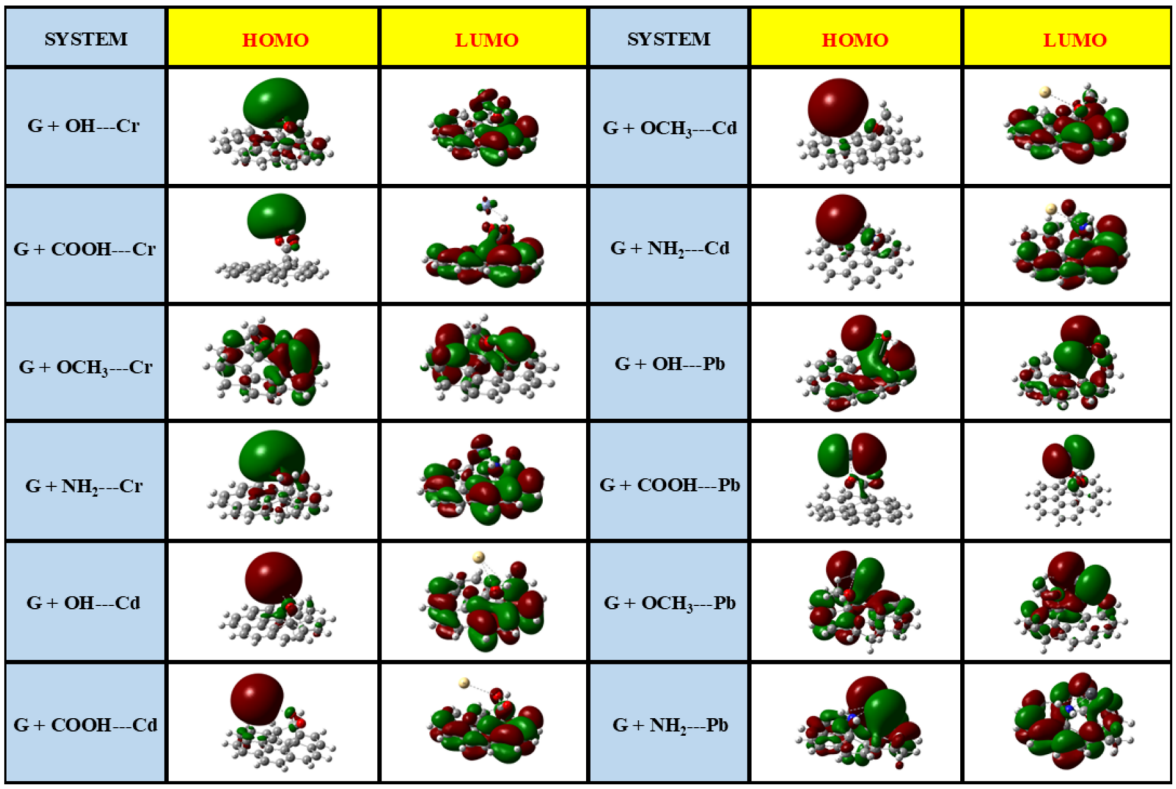

Fig. 13 Visualization of HOMO and LUMO orbitals in metal-adsorbed complexes.

orbital mixing. Meanwhile, –COOH shows moderate orbital interaction, whereas $–OCH_3$ exhibits scattered and localized orbital, indicating weak physisorption. In Cd and Pb complexes, the LUMO is predominantly spread near the metal and COOH group, facilitating strong orbital overlap, while the OH group shows similar localization, though slightly weaker. The methoxy ($–OCH_3$) functionalization exhibits a more delocalized HOMO–LUMO spread for all three metals, pointing to weak interactions and physisorption. The amine ($–NH_2$) group presents moderate HOMO–LUMO overlap, leading to weak chemisorption for Cd, whereas for Pb it exhibits slightly stronger orbital interaction. Overall, COOH-functionalized graphene demonstrates the most effective adsorption across all cases due to highly localized HOMO–LUMO densities, followed by OH and NH_2, while OCH_3 remains the least effective, with widely spread orbitals indicating weak physisorption.

5.3 Global reactivity indices, adsorption energies and Gibbs free energy

Electron affinity is the measure of how easily a substance can capture electrons, with metals having higher electron affinity accepting them more readily.[34] Based on the values, we can establish the following order: Cr (3.335 eV) > Pb (2.979 eV) > Cd (0.722 eV). Metal reactivity is influenced by electronegativity, as shown in Table 2, where Pb has the lowest value followed by Cd and Cr. Since lower electronegativity promotes faster electron equilibrium and greater reactivity, Pb is expected to interact more readily with the carbon surface compared to Cr. Furthermore, the adsorption tendency of metals on an adsorbent can also be understood through global hardness, where metals with lower hardness are more likely to be captured by the adsorbent. The analysed data indicates that lead exhibits the lowest hardness value, whereas cadmium has the highest. Another important factor, chemical potential (μ) plays a important role in determining the electron density exchange between heavy metals and adsorbent surfaces. A lower chemical potential corresponds to a greater tendency for electron donation. Based on the information shown in Table 2, it is confirmed that chromium, having the lowest chemical potential of −4.03, will accept electrons more easily. This facilitates stronger adsorption, while lead, which has the highest chemical potential, will show minimal adsorption. An indicator of a molecule's electrophilicity is its electrophilicity index (ω). Surfaces with lower ω values tend to transfer electrons to metals, enhancing their adsorption efficiency. The obtained results indicate that the electrophilicity index (ω) decreases in the order: graphitefunctionalise with OH (11.5) > OCH_3 (11.3) > NH_2 (10.9) > COOH (10.8) > non-functionalized graphite (10.3).

The interaction energies (ΔE_{bind}), enthalpy changes (ΔH) and Gibbs free energies (ΔG) were estimated to examine the affinity of metal ions toward carbon-based surfaces (Table 3). From the ΔE_{bind} values, it is evident that the interaction strength between metal ions and adsorption matrices is highest for Cr, followed by Pb and Cd. In spite of the negative values, the adsorption energy for Cd points toward the development of weak interactions, most likely electrostatic in nature, which is consistent

Table 2 FMO and global reactivity indices of the complexes. All the values are in eV

S. no	Complex	HOMO	LUMO	E_g	IP	EA	χ	η	S	μ	ω	N
1	G	−5.18	−2.0	3.18	5.18	2.0	3.59	1.59	−3.59	0.79	10.3	0.1
2	G + NH_2	−5.29	−2.11	3.18	5.29	2.11	3.7	1.59	−3.7	0.79	10.9	0.09
3	G + OH	−5.39	−2.2	3.19	5.39	2.2	3.8	1.59	−3.8	0.8	11.5	0.09
4	G + COOH	−5.28	−2.13	3.15	5.28	2.13	3.71	1.57	−3.71	0.79	10.8	0.09
5	G + OCH_3	−5.36	−2.14	3.22	5.36	2.14	3.75	1.61	−3.75	0.81	11.3	0.09
6	G···Cr	−4.42	−1.95	2.47	4.42	1.95	3.19	1.24	−3.19	0.62	6.27	0.16
7	G + COOH···Cr	−3.9	−2.38	1.52	3.9	2.38	3.14	0.76	−3.14	0.38	3.75	0.27
8	G + OCH_3···Cr	−4.23	−1.78	2.46	4.23	1.78	3.01	1.23	−3.01	0.61	5.55	0.18
9	G + NH_2···Cr	−3.35	−2.37	0.98	3.35	2.37	2.86	0.49	−2.86	0.24	2.0	0.5
10	G + OH···Cr	−3.51	−2.49	1.02	3.51	2.49	3.0	0.51	−3.0	0.26	2.3	0.44
11	G···Cd	−5.26	−2.1	3.16	5.26	2.1	3.68	1.58	−3.68	0.79	10.7	0.09
12	G + COOH···Cd	−5.02	−2.22	2.8	5.02	2.22	3.62	1.4	−3.62	0.7	9.15	0.11
13	G + OCH_3···Cd	−4.89	−2.26	2.63	4.89	2.26	3.57	1.31	−3.57	0.66	8.39	0.12
14	G + NH_2···Cd	−4.74	−2.25	2.49	4.74	2.25	3.5	1.24	−3.5	0.62	7.6	0.13
15	G + OH···Cd	−4.97	−2.32	2.65	4.97	2.32	3.64	1.32	−3.64	0.66	8.78	0.11
16	G···Pb	−4.32	−1.96	2.36	4.32	1.96	3.14	1.18	−3.14	0.59	5.82	0.17
17	G + COOH···Pb	−3.49	−2.5	0.99	3.49	2.5	3.0	0.5	−3.0	0.25	2.23	0.45
18	G + OCH_3···Pb	−3.66	−1.99	1.67	3.66	1.99	2.83	0.84	−2.83	0.42	3.35	0.3
19	G + NH_2···Pb	−3.32	−2.17	1.15	3.32	2.17	2.74	0.57	−2.74	0.29	2.16	0.46
20	G + OH···Pb	−5.08	−2.18	2.9	5.08	2.18	3.63	1.45	−3.63	0.72	9.56	0.1

with the minimal alteration in graphite's band gap after adsorption. Among the functionalized graphite surfaces, OCH_3 shows the highest binding energy for chromium, whereas COOH-functionalized graphite exhibits the least interaction. In the case of lead, the strongest binding energy is observed with OH-functionalized graphite, while the lowest interaction is seen with COOH-functionalized graphite. Similarly, cadmium exhibits the maximum binding energy with NH_2-functionalized graphite, whereas the least interaction is found with pristine graphite. The enthalpy change provides valuable insight into the nature of the reaction. An endothermic adsorption process is indicated by a positive ΔH, while an exothermic reaction with energy release is suggested by a negative ΔH. Likewise, the spontaneity of an interaction is indicated by the change in the Gibbs free energy (ΔG), where $\Delta G < 0$ denotes a spontaneous process. The findings indicate that each metal exhibit interactions with all graphite-like surfaces, accompanied by release of energy. Likewise, all interaction proceeds spontaneously, except for the case of Cd adsorption on a non-functionalized graphite surface.

Table 3 Calculated values of interaction energy (ΔE_{bind}), enthalpy (ΔH) and Gibbs free energy (ΔG) for all considered complexes

Complexes	ΔE_{bind} (kcal mol^{-1})	ΔH (kcal mol^{-1})	ΔG (kcal mol^{-1})
G···Cr	−81.584	−82.886	−73.608
G + NH_2···Cr	−54.614	−54.583	−47.195
G + OH···Cr	−46.770	−47.875	−39.151
G + COOH···Cr	−45.685	−45.660	−38.291
G + OCH_3···Cr	−93.187	−94.166	−84.412
G···Cd	−4.906	−4.624	0.826
G + NH_2···Cd	−8.269	−7.862	−1.345
G + OH···Cd	−7.704	−7.366	−1.018
G + COOH···Cd	−6.744	−6.406	−0.222
G + OCH_3···Cd	−7.874	−7.536	−1.477
G···Pb	−41.815	−42.313	−34.112
G + NH_2···Pb	−40.499	−41.390	−32.757
G + OH···Pb	−96.233	−97.401	−90.330
G + COOH···Pb	−25.307	−26.537	−19.253
G + OCH_3···Pb	−39.488	−40.656	−32.431

5.4 QTAIM analysis

The chemical bonding properties of complexes created by the interaction of metals with adsorbent surfaces were examined using Bader's Quantum Theory of Atoms in Molecules (QTAIM). The Laplacian of electron density $\nabla^2\rho(r)$, electron density $\rho(r)$, potential energy distribution $V(r)$, kinetic energy density $G(r)$, total energy density $H(r)$, electron localisation function (ELF), localised orbital locator (LOL), and the energy ratio $-G(r)/V(r)$ are among the significant descriptors examined using QTAIM analysis. Table 4 contains the detailed values of topological parameters corresponding to all interactions. The interaction strength is directly related to the electronic density $\rho(r)$ at the bond critical point (BCP), with higher density values corresponding to stronger interactions.[83] Images illustrating the bond critical points (BCPs) for all complexes are included in SI Section S9. The data indicate that, among non-functionalized graphite surfaces, G···Cr (0.058) and G···Pb (0.057) form stronger interactions than G···Cd (0.008), implying that Cd has the lowest binding affinity to pure graphite. The enhancement in $\rho(r)$ values compared to pure graphite demonstrates that functionalization reinforces metal adsorption. The functional group on the graphite-like surface plays an essential role in determining the strength of interactions during the adsorption of Cd, Cr, and Pb metals. NH_2 exhibits the strongest interaction with Cd, while for Cr, both NH_2 and COOH enhance binding, with NH_2 having a slight advantage. Among Pb complexes, OH shows the highest interaction, confirming Pb's strong affinity for OH-functionalized graphite like surface. If the Laplacian of

Table 4 Topological parameters derived from bond critical points (BCPs) of the interactions which are expressed in atomic units (a.u.)

Molecule	Bond	$r(r)$	$G(r)$	$V(r)$	$-G(r)/V(r)$	$H(r)$	$\nabla^2 r(r)$	ELF	LOL	Interaction type
G⋯Cr	H–Cr	0.058	0.066	−0.08	0.85	−0.01	0.216	0.125	0.274	Partially covalent
G + COOH⋯Cr	O–Cr	0.085	0.085	−0.15	0.561	−0.01	0.527	0.1	0.25	Partially covalent
G + OCH_3⋯Cr	O–Cr	0.051	0.075	−0.08	0.974	0.00	0.291	0.069	0.214	Electrostatic
G + NH_2⋯Cr	N–Cr	0.086	0.113	−0.13	0.844	−0.02	0.37	0.153	0.298	Partially covalent
G + OH⋯Cr	O–Cr	0.078	0.127	−0.13	0.943	−0.01	0.477	0.092	0.242	Partially covalent
G⋯Cd	H–Cd	0.008	0.004	−0	1.026	0.00	0.015	0.068	0.214	Electrostatic
G + COOH⋯Cd	O–Cd	0.01	0.006	−0.01	1.048	0.00	0.025	0.046	0.18	Electrostatic
G + OCH_3⋯Cd	O–Cd	0.011	0.007	−0.01	1.015	0.00	0.027	0.053	0.191	Electrostatic
G + NH_2⋯Cd	N–Cd	0.013	0.007	−0.01	0.988	0.00	0.027	0.085	0.233	Electrostatic
G + OH⋯Cd	O–Cd	0.01	0.006	−0.01	1.001	0.00	0.023	0.054	0.193	Electrostatic
G⋯Pb	C–Pb	0.057	0.019	−0.03	0.608	−0.01	0.111	0.554	0.489	Partially covalent
G + COOH⋯Pb	O–Pb	0.05	0.025	−0.03	0.872	0.00	0.193	0.285	0.332	Electrostatic
G + OCH_3⋯Pb	O–Pb	0.054	0.027	−0.03	0.847	0.00	0.204	0.307	0.342	Electrostatic
G + NH_2⋯Pb	N–Pb	0.058	0.022	−0.03	0.711	−0.01	0.171	0.494	0.425	Partially covalent
G + OH⋯Pb	O–Pb	0.117	0.059	−0.08	0.733	−0.02	0.496	0.632	0.416	Partially covalent

electron density $\nabla^2\rho(r)$ is negative, it suggests a covalent bond, whereas a positive value indicates a non-covalent interaction. The positive values of $\nabla^2\rho(r)$ across all investigated complexes confirm that they engage in non-covalent interactions ($\nabla^2\rho(r) > 0$). Additionally, the values of $\nabla^2\rho(r)$ and $H(r)$ allow for the identification and classification of different intermolecular interactions. An interaction is electrostatic when both $\nabla^2\rho(r)$ and $H(r)$ are positive, whereas a positive $\nabla^2\rho(r)$ paired with a negative $H(r)$ signifies a partial covalent character.[78,81] The tabular data analysis indicates that, depending on the metal's interaction with the matrix, complexes can show both electrostatic and partially covalent connections. Based on a detailed evaluation of binding energies, frontier molecular orbital interactions, quantum chemical descriptors, and QTAIM parameters, the adsorption affinity on carbonaceous materials ranks in the order: Pb > Cr > Cd.

6. Summary

The adsorption studies revealed that Pb^{2+} consistently achieved the greatest uptake across all investigated adsorbents, followed by Cd^{2+} and lastly Cr^{6+}. Notably, BN char displayed outstanding adsorption performance despite its modest BET surface area, a behaviour credited to its rich oxygen-containing functional groups and well-developed layered mesoporous framework that improved metal accessibility. These experimental results largely correspond with the theoretical predictions, although minor variations remain in the calculated order of binding strengths. An overall summary of the theoretical calculations is provided in Table 5.

According to DFT results, Pb^{2+} and Cd^{2+} bind strongly and exothermically to oxygen-rich surfaces, whereas Cr^{6+} appeared to show unexpectedly high affinity in gas-phase calculations. This, however, does not match the experimental outcome. The reason lies in the fact that theoretical gas-phase models do not consider hydration effects, solvation energies, or ionic forms present in real solutions. At pH around 4, Cr^{6+} mainly exists as hydrated chromate or dichromate anions with large solvation shells, which stabilize them in water and reduce their effective affinity for carbon surfaces. Thus, while gas-phase models suggest strong binding, the weak adsorption of Cr^{6+} observed experimentally arises because these models do not account for desolvation effects. The HOMO–LUMO analysis provides further insight into these trends. For Pb^{2+} and Cr^{6+}, significant orbital overlap with –OH and $-NH_2$ surface groups were observed, suggesting chemisorptive interactions mediated by partial charge transfer. Conversely, Cd^{2+} exhibited more diffuse orbital distribution with limited overlap, consistent with predominantly electrostatic or ionic interactions. These theoretical findings align closely with experimental data, where Pb^{2+} demonstrated the strongest uptake through surface complexation, while Cd^{2+} adsorption was comparatively moderate and strongly reliant on functional group availability. However, the higher calculated reactivity for Cr compared with Cd does not translate into greater uptake experimentally. As noted earlier, this deviation stems from aqueous-phase influences that gas-phase orbital models fail to capture.

Global reactivity descriptors provide additional confirmation of these trends. Pb^{2+} was found to have the lowest chemical hardness and the narrowest band gap, designating it as the most polarizable and chemically "soft" ion, which correlates well with its strong affinity for surfaces and superior experimental uptake. Conversely, Cd^{2+} possessed the largest band gap and highest hardness, classifying it as a chemically "harder" species with reduced reactivity, consistent with its weaker adsorption in practice. Although Cr^{6+} demonstrated high electron affinity and electronegativity, which theoretically suggest strong electron-accepting capacity, this tendency is suppressed in aqueous systems due to extensive solvation, leading to poor adsorption performance.

Thermodynamic parameters provide further clarification of the adsorption behaviour. All systems exhibited exothermic enthalpy changes ($\Delta H < 0$) and negative free energy ($\Delta G < 0$), confirming spontaneity on functionalized surfaces. For Pb^{2+} and Cr^{6+}, adsorption was consistently favourable across different functional groups, whereas Cd^{2+} binding was only weakly exothermic and became thermodynamically spontaneous only in the presence of surface functionalities,

Table 5 Comparative analysis of adsorption affinity, HOMO–LUMO properties, global reactivity descriptors, adsorption energies, and QTAIM analysis for Pb, Cd, and Cr

Analysis type	Key parameters	Lead	Cadmium	Chromium	Conclusion
Experimental affinity order	NA	Highest	Moderate	Lowest	Pb > Cd > Cr, Pb binds most effectively in real aqueous systems, followed by Cd and then Cr
Theoretical affinity (ΔE_{bind}) order		Moderate	Weakest	Strongest	Cr > Pb > Cd, DFT predicts strongest binding for Cr, highlighting a discrepancy with experiment due to solvation and speciation effects not accounted for in the gas-phase calculation
HOMO–LUMO analysis	Functional groups	Strong (on –COOH and –NH_2)	Weak; scattered orbitals	Strong (on –NH_2 and –OH)	NA
	Carboxyl (–COOH)	Strong chemisorption LUMO spread near metal & group. Strong orbital overlap	Strong chemisorption LUMO spread near metal & group. Strong orbital overlap	Moderate chemisorption Moderate orbital interaction	Most effective. Promotes strong chemisorption for all metals due to highly localized orbital densities
	Amino (–NH_2)	Strong chemisorption Stronger orbital interaction	Weak chemisorption Moderate HOMO–LUMO overlap	Strong chemisorption Significant LUMO delocalization across Cr and surface	Highly effective. Excellent for Pb and Cr, weaker for Cd. Leads to chemisorption
	Hydroxyl (–OH)	Strong chemisorption Localization similar to COOH, slightly weaker	Weak chemisorption Localization similar to COOH, slightly weaker	Strong chemisorption Significant LUMO delocalization across Cr and surface	Effective. Good performance across all metals, promoting chemisorption
	Methoxy (–OCH_3)	Physisorption Delocalized, scattered orbitals. Weak interaction	Physisorption Delocalized, scattered orbitals. Weak interaction	Physisorption Scattered and localized orbitals. Weak interaction	Least effective. Only promotes weak physisorption for all metals
	Band gap	0.676	5.283	1.393	Largest band gap (Cd) indicates high stability and low intrinsic reactivity (a “hard” ion) whereas smallest band gap indicates low stability, high polarizability, and high intrinsic reactivity (a “soft” ion)
Global reactivity descriptors	Electron affinity (EA)	Moderate	Lowest	Highest	Cr > Pb > Cd, Cr has highest tendency to gain electrons
	Electronegativity (χ)	Lowest	Moderate	Highest	Pb is expected to interact more readily with the carbon surface compared to Cr
	Chemical hardness (η)	Lowest	Highest	Moderate	Pb is the “softest” (most polarizable, most reactive) meanwhile Cd is the “hardest” (least reactive)

Table 5 (*Contd.*)

Analysis type	Key parameters	Lead	Cadmium	Chromium	Conclusion
	Chemical potential (μ)	Highest (least negative)	Moderate	Lowest (most negative)	Cr has the highest tendency to accept electrons (strongest electrophile) whereas Pb has the lowest tendency to accept electrons
Adsorption energies and thermodynamic parameters	Strongest interaction with	G + OH, $\Delta E_{bind} = -96.233$	G + NH_2, $\Delta E_{bind} = -8.269$	G + OCH_3, $\Delta E_{bind} = -93.187$	The optimal functional group for binding is metal-specific. Hydroxyl groups are paramount for Pb, amine for Cd, and methoxy for Cr
	Weakest interaction with	G + COOH, $\Delta E_{bind} = -25.307$	G (pristine), $\Delta E_{bind} = -4.906$	G + COOH, $\Delta E_{bind} = -45.685$	Carboxyl groups show the weakest binding for Pb and Cr, while pristine graphite provides the least favourable interaction for Cd
	Thermodynamic nature	Strongly exothermic ($\Delta H < 0$) and spontaneous ($\Delta G < 0$) for all surfaces	Weakly exothermic ($\Delta H < 0$). Spontaneous ($\Delta G < 0$) on functionalized surfaces. Non-spontaneous ($\Delta G > 0$) on pristine graphite	Strongly exothermic ($\Delta H < 0$) and spontaneous ($\Delta G < 0$) for all surfaces	While Pb and Cr interactions are strongly favourable across surfaces, Cd adsorption is only weakly exothermic and requires functionalization for spontaneity
QTAIM analysis	Interaction type	Partially covalent (with –OH, –NH_2)	Purely electrostatic	Partially covalent (with –COOH, –NH_2, –OH)	Pb and Cr tend to form stronger, charge-sharing bonds (chemisorption) with certain groups, while Cd interactions are primarily ionic/electrostatic (physisorption)

underlining the decisive influence of surface chemistry. This interpretation is corroborated by FTIR evidence, showing that BN char produced at 400 °C retained a higher density of oxygenated groups, thereby enabling stronger Cd^{2+} adsorption compared with PJ biochar. QTAIM analysis further clarified the interaction mechanisms. Pb^{2+} and Cr^{6+} exhibited features of partial covalent bonding with –OH and $–NH_2$ groups, indicative of chemisorption, whereas Cd^{2+} binding was predominantly electrostatic in nature, characteristic of physisorption. These theoretical results closely parallel the experimental observations: Pb^{2+} adsorption is driven by strong, stable surface complexation, while Cd^{2+} uptake remains less efficient due to its dependence on weaker ionic forces. Together, the theoretical and experimental results show that adsorption depends more on surface chemistry and ion characteristics than on surface area.

7. Conclusion

This work examines the adsorption of Pb^{2+}, Cd^{2+}, and Cr^{6+} on carbon-based adsorbents with different surface functionalities by combining theoretical calculations with actual research. The comparative analysis of their adsorption capacities revealed distinct differences in their removal efficiencies for the three metal ions. Banana char (BN char) demonstrated the best results for removing chromium, with an adsorption capacity of 16.50 ± 60 mg g^{-1} and a removal efficiency of $16.50 \pm 60\%$. This was followed by PJ biochar (12.64 ± 40 mg g^{-1}), GAC-CS (10.96 ± 40 mg g^{-1}), and GAC (9.40 ± 20 mg g^{-1}), indicating a relatively lower affinity of all adsorbents for chromium ions. In the case of cadmium removal, BN char showed exceptional performance with a removal efficiency of $93.08 \pm 40\%$ and an adsorption capacity of 186.16 ± 40 mg g^{-1}, significantly surpassing the other adsorbents. PJ biochar demonstrated moderate efficiency (44.76 ± 0.60 mg g^{-1}), while GAC-CS (36.30 ± 0.60 mg g^{-1}) and GAC (32.5 ± 0.60 mg g^{-1}) were slightly less effective. Regarding lead removal, BN char displayed the efficiency with a removal rate of $63.12 \pm 0.60\%$ and an impressive adsorption capacity of 252.46 ± 0.60 mg g^{-1}. PJ biochar also showed substantial removal ($96.47 \pm 0.80\%$, 192.94 ± 0.80 mg g^{-1}), whereas GAC-CS and GAC achieved moderate adsorption capacities of 51.68 ± 0.40 mg g^{-1} and 49.20 ± 0.40 mg g^{-1}, respectively. Although DFT computations indicate a binding affinity order of Pb > Cr > Cd, experimental findings frequently reveal a different trend: Pb > Cd > Cr. The disagreement between theoretical and experimental data primarily stems from the limitations of simulations in accounting for solvent-mediated and environmental effects present in real systems. Overall, the data indicate that, lead exhibited the highest removal efficiency across all adsorbents, followed by cadmium, while chromium consistently showed the lowest removal. This trend implies that lead ions bind more strongly with the surface functional groups of these carbon-based materials. The combined theoretical and experimental analyses present a consistent picture: Pb^{2+} adsorption is both thermodynamically and electronically favoured, accounting for its superior uptake; Cd^{2+}, limited by greater hardness and weaker orbital overlap, shows only moderate adsorption that improves with surface functionalization; whereas Cr^{6+}, despite strong binding predicted in vacuum models, exhibits poor removal in practice due to dominant solvation and speciation effects in aqueous media. Theoretical data from DFT calculations also suggest, surface chemistry and adsorbent structure play crucial roles in determining the selectivity and capacity for heavy metal removal. In this study, the theoretical framework was limited by the omission of explicit solvent representation, which may restrict the accuracy of adsorption predictions. Additionally, aspects such as adsorbent regeneration and long-term durability over multiple cycles were not explored. Future research should aim to incorporate explicit solvent models and molecular dynamics into theoretical simulations, supported by systematic experimental validation. Such an integrated approach can guide the rational design of advanced carbon-based adsorbents for more efficient and sustainable heavy metal removal.

Conflicts of interest

The authors declare that they have no known competing financial interests or personal relationships that could have appeared to influence the work reported in this paper.

Data availability

All data generated or analyzed during this study are included in the SI accompanying this article. Supplementary information is available. See DOI: https://doi.org/10.1039/d5ra03863d.

Acknowledgements

The authors sincerely acknowledge the support of Vellore Institute of Technology, Vellore for providing laboratory facilities and instrumental assistance in conducting these experiments. We also are thankful to SAS-SIF for their instrumental support in the material characterization. The authors also wish to express their gratitude to the Centre for Nanotechnology Research (CNR) for their provision of Raman spectra analysis. Additionally, our sincere thanks go to the School of Biosciences and Technology (SBST) and the Centre for Materials Characterisation and Techniques for offering SEM and FE-SEM facilities for the material analysis. We would like to thank the Technology Business Incubator (TBI) for facilitating the analysis of heavy metals through Atomic Absorption Spectroscopy (AAS). We are also deeply thankful to Dr Senthil Kumar Annamalai, Director of the CO_2 Research and Green Technology Centre, for generously providing the PJ biochar sample used in this study. We would also like to thank Dr Kamlesh Chaudhari, Principal Scientist, International Centre for Clean Water (ICCW), IIT-M Research Park, for providing additional support with the instrumentation facilities available at ICCW.

References

1 D. Kołodyńska, J. Krukowska and P. Thomas, Comparison of Sorption and Desorption Studies of Heavy Metal Ions from

Biochar and Commercial Active Carbon, *Chem. Eng. J.*, 2017, **307**, 353–363, DOI: 10.1016/j.cej.2016.08.088.

2 P. B. Angon, M. S. Islam, Shreejana KC, A. Das, N. Anjum, A. Poudel and S. A. Suchi, Sources, Effects and Present Perspectives of Heavy Metals Contamination: Soil, Plants and Human Food Chain, *Heliyon*, 2024, **10**(7), e28357, DOI: 10.1016/j.heliyon.2024.e28357.

3 L. C. Rai, J. P. Gaur and H. D. Kumar, Phycology and Heavy-Metal Pollution, *Biol. Rev.*, 1981, **56**(2), 91–151, DOI: 10.1111/j.1469-185X.1981.tb00345.x.

4 F. Fu and Q. Wang, Removal of Heavy Metal Ions from Wastewaters: A Review, *J. Environ. Manage.*, 2011, **92**(3), 407–418, DOI: 10.1016/j.jenvman.2010.11.011.

5 B. Viard, F. Pihan, S. Promeyrat and J.-C. Pihan, Integrated Assessment of Heavy Metal (Pb, Zn, Cd) Highway Pollution: Bioaccumulation in Soil, Graminaceae and Land Snails, *Chemosphere*, 2004, **55**(10), 1349–1359, DOI: 10.1016/j.chemosphere.2004.01.003.

6 F. C. C, T. Kamalesh, P. S. Kumar and G. Rangasamy, A Critical Review on the Sustainable Approaches for the Removal of Toxic Heavy Metals from Water Systems, *Ind. Eng. Chem. Res.*, 2023, **62**(22), 8575–8601, DOI: 10.1021/acs.iecr.3c00709.

7 N. A. A. Qasem, R. H. Mohammed and D. U. Lawal, Removal of Heavy Metal Ions from Wastewater: A Comprehensive and Critical Review, *npj Clean Water*, 2021, **4**(1), 36, DOI: 10.1038/s41545-021-00127-0.

8 Ç. Kırbıyık, A. E. Pütün and E. Pütün, Comparative Studies on Adsorptive Removal of Heavy Metal Ions by Biosorbent, Bio-Char and Activated Carbon Obtained from Low Cost Agro-Residue, *Water Sci. Technol.*, 2016, **73**(2), 423–436, DOI: 10.2166/wst.2015.504.

9 F. Akhter, F. M. Zoppas, M. Soomro, A. S. Jatoi, F. Noureen, M. N. Akhtar and F. Mehreen, Carbon-Based Sorbets for Heavy Metal Removal from Aqueous Solution, Discrepancies, and Future Prospects: A State-of-the-Art Review, *Biomass Convers. Biorefin.*, 2023, **13**(12), 10343–10359, DOI: 10.1007/s13399-021-01866-3.

10 K. Pyrzyńska and M. Bystrzejewski, Comparative Study of Heavy Metal Ions Sorption onto Activated Carbon, Carbon Nanotubes, and Carbon-Encapsulated Magnetic Nanoparticles, *Colloids Surf., A*, 2010, **362**(1–3), 102–109, DOI: 10.1016/j.colsurfa.2010.03.047.

11 Y. Fei and Y. H. Hu, Design, Synthesis, and Performance of Adsorbents for Heavy Metal Removal from Wastewater: A Review, *J. Mater. Chem. A*, 2022, **10**(3), 1047–1085, DOI: 10.1039/D1TA06612A.

12 B. Wang, J. Lan, C. Bo, B. Gong and J. Ou, Adsorption of Heavy Metal onto Biomass-Derived Activated Carbon: Review, *RSC Adv.*, 2023, **13**(7), 4275–4302, DOI: 10.1039/D2RA07911A.

13 M. S. Soffian, F. Z. Abdul Halim, F. Aziz, M. A. Rahman, M. A. Mohamed Amin and D. N. Awang Chee, Carbon-Based Material Derived from Biomass Waste for Wastewater Treatment, *Environ. Adv.*, 2022, **9**, 100259, DOI: 10.1016/j.envadv.2022.100259.

14 H. P. S. A. Khalil, N. A. S. Aprilia, A. H. Bhat, M. Jawaid, M. T. Paridah and D. Rudi, A Jatropha Biomass as Renewable Materials for Biocomposites and Its Applications, *Renewable Sustainable Energy Rev.*, 2013, **22**, 667–685, DOI: 10.1016/j.rser.2012.12.036.

15 S. R. Mousavi, M. Asghari, N. M. Mahmoodi and I. Salahshoori, Water Decolorization and Antifouling Melioration of a Novel PEBA1657/PES TFC Membrane Using Chitosan-Decorated Graphene Oxide Fillers, *J. Environ. Chem. Eng.*, 2023, **11**(3), 109955, DOI: 10.1016/j.jece.2023.109955.

16 I. Pet, M. N. Sanad, M. Farouz, M. M. ElFaham, A. El-Hussein, M. S. A. El-sadek, R. A. Althobiti and A. Ioanid, Review: Recent Developments in the Implementation of Activated Carbon as Heavy Metal Removal Management, *Water Conserv. Sci. Eng.*, 2024, **9**(2), 62, DOI: 10.1007/s41101-024-00287-3.

17 A. Gul, A. Ma'amor, N. G. Khaligh and N. Muhd Julkapli, Recent Advancements in the Applications of Activated Carbon for the Heavy Metals and Dyes Removal, *Chem. Eng. Res. Des.*, 2022, **186**, 276–299, DOI: 10.1016/j.cherd.2022.07.051.

18 A. Karimah, M. R. Ridho, S. S. Munawar, D. S. Adi, Ismadi, R. Damayanti, B. Subiyanto, W. Fatriasari and A. Fudholi, A Review on Natural Fibers for Development of Eco-Friendly Bio-Composite: Characteristics, and Utilizations, *J. Mater. Res. Technol.*, 2021, **13**, 2442–2458, DOI: 10.1016/j.jmrt.2021.06.014.

19 N. Mohamad Nor, L. C. Lau, K. T. Lee and A. R. Mohamed, Synthesis of Activated Carbon from Lignocellulosic Biomass and Its Applications in Air Pollution Control—a Review, *J. Environ. Chem. Eng.*, 2013, **1**(4), 658–666, DOI: 10.1016/j.jece.2013.09.017.

20 H. Chakhtouna, H. Benzeid, N. Zari, A. e. k. Qaiss and R. Bouhfid, Recent Advances in Eco-Friendly Composites Derived from Lignocellulosic Biomass for Wastewater Treatment, *Biomass Convers. Biorefin.*, 2024, **14**(11), 12085–12111, DOI: 10.1007/s13399-022-03159-9.

21 P. González-García, Activated Carbon from Lignocellulosics Precursors: A Review of the Synthesis Methods, Characterization Techniques and Applications, *Renewable Sustainable Energy Rev.*, 2018, **82**, 1393–1414, DOI: 10.1016/j.rser.2017.04.117.

22 H. P. S. Abdul Khalil, Y. Davoudpour, M. N. Islam, A. Mustapha, K. Sudesh, R. Dungani and M. Jawaid, Production and Modification of Nanofibrillated Cellulose Using Various Mechanical Processes: A Review, *Carbohydr. Polym.*, 2014, **99**, 649–665, DOI: 10.1016/j.carbpol.2013.08.069.

23 Suhas, P. J. M. Carrott and M. M. L. Ribeiro Carrott, Lignin – from Natural Adsorbent to Activated Carbon: A Review, *Bioresour. Technol.*, 2007, **98**(12), 2301–2312, DOI: 10.1016/j.biortech.2006.08.008.

24 D. L. Klass, Energy Consumption, Reserves, Depletion, and Environmental Issues, in *Biomass for Renewable Energy, Fuels, and Chemicals*, Elsevier, 1998, pp. 1–27, DOI: 10.1016/B978-012410950-6/50003-9.

25 G. Kwon, A. Bhatnagar, H. Wang, E. E. Kwon and H. Song, A Review of Recent Advancements in Utilization of Biomass and Industrial Wastes into Engineered Biochar, *J. Hazard. Mater.*, 2020, **400**, 123242, DOI: 10.1016/j.jhazmat.2020.123242.

26 H. He, R. Zhang, P. Zhang, P. Wang, N. Chen, B. Qian, L. Zhang, J. Yu and B. Dai, Functional Carbon from Nature: Biomass-Derived Carbon Materials and the Recent Progress of Their Applications, *Adv. Sci.*, 2023, **10**(16), 2205557, DOI: 10.1002/advs.202205557.

27 A. Dashti, M. Raji, A. Azarafza, A. Baghban, A. H. Mohammadi and M. Asghari, Rigorous Prognostication and Modeling of Gas Adsorption on Activated Carbon and Zeolite-5A, *J. Environ. Manage.*, 2018, **224**, 58–68, DOI: 10.1016/j.jenvman.2018.06.091.

28 H. Haykiri-Acma, S. Yaman and S. Kucukbayrak, Gasification of Biomass Chars in Steam–Nitrogen Mixture, *Energy Convers. Manag.*, 2006, **47**(7–8), 1004–1013, DOI: 10.1016/j.enconman.2005.06.003.

29 K. Raveendran, Adsorption Characteristics and Pore-Development of Biomass-Pyrolysis Char, *Fuel*, 1998, **77**(7), 769–781, DOI: 10.1016/S0016-2361(97)00246-9.

30 V. Thakur, E. Sharma, A. Guleria, S. Sangar and K. Singh, Modification and Management of Lignocellulosic Waste as an Ecofriendly Biosorbent for the Application of Heavy Metal Ions Sorption, *Mater. Today Proc.*, 2020, **32**, 608–619, DOI: 10.1016/j.matpr.2020.02.756.

31 S.-A. Sajjadi, A. Meknati, E. C. Lima, G. L. Dotto, D. I. Mendoza-Castillo, I. Anastopoulos, F. Alakhras, E. I. Unuabonah, P. Singh and A. Hosseini-Bandegharaei, A Novel Route for Preparation of Chemically Activated Carbon from Pistachio Wood for Highly Efficient Pb(II) Sorption, *J. Environ. Manage.*, 2019, **236**, 34–44, DOI: 10.1016/j.jenvman.2019.01.087.

32 O. Ioannidou and A. Zabaniotou, Agricultural Residues as Precursors for Activated Carbon Production—A Review, *Renewable Sustainable Energy Rev.*, 2007, **11**(9), 1966–2005, DOI: 10.1016/j.rser.2006.03.013.

33 A. E. Pütün, N. Özbay, E. P. Önal and E. Pütün, Fixed-Bed Pyrolysis of Cotton Stalk for Liquid and Solid Products, *Fuel Process. Technol.*, 2005, **86**(11), 1207–1219, DOI: 10.1016/j.fuproc.2004.12.006.

34 M. Fan, Steam Activation of Chars Produced from Oat Hulls and Corn Stover, *Bioresour. Technol.*, 2004, **93**(1), 103–107, DOI: 10.1016/j.biortech.2003.08.016.

35 Y. Wang and R. Liu, Comparison of Characteristics of Twenty-One Types of Biochar and Their Ability to Remove Multi-Heavy Metals and Methylene Blue in Solution, *Fuel Process. Technol.*, 2017, **160**, 55–63, DOI: 10.1016/j.fuproc.2017.02.019.

36 S. Vinitnantharat, W. Rattanasirisophon and Y. Ishibashi, Modification of Granular Activated Carbon Surface by Chitosan Coating for Geosmin Removal: Sorption Performances, *Water Sci. Technol.*, 2007, **55**(5), 145–152, DOI: 10.2166/wst.2007.173.

37 S. Kokate, K. Parasuraman and H. Prakash, Adsorptive Removal of Lead Ion from Water Using Banana Stem Scutcher Generated in Fiber Extraction Process, *Results Eng.*, 2022, **14**, 100439, DOI: 10.1016/j.rineng.2022.100439.

38 R. Ashwin, A. MercyVasan and K. Subramanian, Production and Characterization of Biochar from Agro-Forestry-Based Waste Prosopis Juliflora: A Sustainable Amendment for Soil Conditioning, *Biomass Convers. Biorefin.*, 2025, **15**, 20347–20364, DOI: 10.1007/s13399-025-06613-6.

39 A. GuhaRay, M. Guoxiong, A. Sarkar, S. Bordoloi, A. Garg and S. Pattanayak, Geotechnical and Chemical Characterization of Expansive Clayey Soil Amended by Biochar Derived from Invasive Weed Species Prosopis Juliflora, *Innov. Infrastruct. Solut.*, 2019, **4**(1), 44, DOI: 10.1007/s41062-019-0231-2.

40 G. Gayathri and K. B. Uppuluri, The Comprehensive Characterization of Prosopis Juliflora Pods as a Potential Bioenergy Feedstock, *Sci. Rep.*, 2022, **12**(1), 18586, DOI: 10.1038/s41598-022-22482-9.

41 C. Diaz-Uribe, J. Ortiz, F. Duran, W. Vallejo and J. Fals, Methyl Orange Adsorption on Biochar Obtained from Prosopis Juliflora Waste: Thermodynamic and Kinetic Study, *ChemEngineering*, 2023, **7**(6), 114, DOI: 10.3390/chemengineering7060114.

42 P. Subramanian, S. Pakkiyam, K. Pandian, S. Chinnathambi and M. Jayaraman, Preparation and Modification of Prosopis Juliflora Biochar and Pb (II) Removal from Aqueous Solutions, *Biomass Convers. Biorefin.*, 2025, **15**(1), 421–435, DOI: 10.1007/s13399-024-05575-5.

43 O. A. Ekpete, A. C. Marcus and V. Osi, Preparation and Characterization of Activated Carbon Obtained from Plantain (Musa Paradisiaca) Fruit Stem, *J. Chem.*, 2017, **2017**, 1–6, DOI: 10.1155/2017/8635615.

44 E. Misran, O. Bani, E. M. Situmeang and A. S. Purba, Banana Stem Based Activated Carbon as a Low-Cost Adsorbent for Methylene Blue Removal: Isotherm, Kinetics, and Reusability, *Alexandria Eng. J.*, 2022, **61**(3), 1946–1955, DOI: 10.1016/j.aej.2021.07.022.

45 B. Lapo, J. J. Bou, J. Hoyo, M. Carrillo, K. Peña, T. Tzanov and A. M. Sastre, A Potential Lignocellulosic Biomass Based on Banana Waste for Critical Rare Earths Recovery from Aqueous Solutions, *Environ. Pollut.*, 2020, **264**, 114409, DOI: 10.1016/j.envpol.2020.114409.

46 S. Xu, W. Yu, S. Liu, C. Xu, J. Li and Y. Zhang, Adsorption of Hexavalent Chromium Using Banana Pseudostem Biochar and Its Mechanism, *Sustainability*, 2018, **10**(11), 4250, DOI: 10.3390/su10114250.

47 J. L. Guimarães, E. Frollini, C. G. da Silva, F. Wypych and K. G. Satyanarayana, Characterization of Banana, Sugarcane Bagasse and Sponge Gourd Fibers of Brazil, *Ind. Crops Prod.*, 2009, **30**(3), 407–415, DOI: 10.1016/j.indcrop.2009.07.013.

48 N. Salamun, S. Triwahyono, A. A. Jalil, Z. A. Majid, Z. Ghazali, N. A. F. Othman and D. Prasetyoko, Surface Modification of Banana Stem Fibers via Radiation Induced Grafting of Poly(Methacrylic Acid) as an Effective Cation Exchanger for Hg (<scp>ii</Scp>), *RSC Adv.*, 2016, **6**(41), 34411–34421, DOI: 10.1039/C6RA03741K.

49 L. Jaber, I. Ihsanullah, I. W. Almanassra, S. N. Backer, A. Abushawish, A. K. A. Khalil, H. Alawadhi, A. Shanableh

and M. A. Atieh, Adsorptive Removal of Lead and Chromate Ions from Water by Using Iron-Doped Granular Activated Carbon Obtained from Coconut Shells, *Sustainability*, 2022, **14**(17), 10877, DOI: 10.3390/su141710877.

50 L. Li, S. Liu and J. Liu, Surface Modification of Coconut Shell Based Activated Carbon for the Improvement of Hydrophobic VOC Removal, *J. Hazard. Mater.*, 2011, **192**(2), 683–690, DOI: 10.1016/j.jhazmat.2011.05.069.

51 L. Yanyan, T. A. Kurniawan, M. Zhu, T. Ouyang, R. Avtar, M. H. Dzarfan Othman, B. T. Mohammad and A. B. Albadarin, Removal of Acetaminophen from Synthetic Wastewater in a Fixed-Bed Column Adsorption Using Low-Cost Coconut Shell Waste Pretreated with NaOH, HNO3, Ozone, and/or Chitosan, *J. Environ. Manage.*, 2018, **226**, 365–376, DOI: 10.1016/j.jenvman.2018.08.032.

52 O. J. Al-sareji, M. Meiczinger, V. Somogyi, R. A. Al-Juboori, R. A. Grmasha, C. Stenger-Kovács, M. Jakab and K. S. Hashim, Removal of Emerging Pollutants from Water Using Enzyme-Immobilized Activated Carbon from Coconut Shell, *J. Environ. Chem. Eng.*, 2023, **11**(3), 109803, DOI: 10.1016/j.jece.2023.109803.

53 E. Arriola-Villaseñor, A. N. Ardila A, Z. Rolando Barrera and J. Hernández, Using Banana Waste Biochar for Simultaneous Removal of Heavy Metals from Raw Real Wastewater from the Electroplating Industry, *Desalin. Water Treat.*, 2023, **314**, 88–102, DOI: 10.5004/dwt.2023.30079.

54 D. Fetjah, L. F. Z. Ainlhout, Z. Idardare, B. Ihssane and L. Bouqbis, Effect of Banana-Waste Biochar and Compost Mixtures on Growth Responses and Physiological Traits of Seashore Paspalum Subjected to Six Different Water Conditions, *Sustainability*, 2022, **14**(3), 1541, DOI: 10.3390/su14031541.

55 A. R. Hidayu and N. Muda, Preparation and Characterization of Impregnated Activated Carbon from Palm Kernel Shell and Coconut Shell for CO2 Capture, *Procedia Eng.*, 2016, **148**, 106–113, DOI: 10.1016/j.proeng.2016.06.463.

56 N. M. Keppetipola, M. Dissanayake, P. Dissanayake, B. Karunarathne, M. A. Dourges, D. Talaga, L. Servant, C. Olivier, T. Toupance, S. Uchida, K. Tennakone, G. R. A. Kumara and L. Cojocaru, Graphite-Type Activated Carbon from Coconut Shell: A Natural Source for Eco-Friendly Non-Volatile Storage Devices, *RSC Adv.*, 2021, **11**(5), 2854–2865, DOI: 10.1039/D0RA09182K.

57 R. Kabir Ahmad, S. Anwar Sulaiman, S. Yusup, S. Sham Dol, M. Inayat and H. Aminu Umar, Exploring the Potential of Coconut Shell Biomass for Charcoal Production, *Ain Shams Eng. J.*, 2022, **13**(1), 101499, DOI: 10.1016/j.asej.2021.05.013.

58 G. Mo, J. Xiao and X. Gao, To Enhance the Cd2+ Adsorption Capacity on Coconut Shell-Derived Biochar by Chitosan Modifying: Performance and Mechanism, *Biomass Convers. Biorefin.*, 2023, **13**(18), 16737–16752, DOI: 10.1007/s13399-021-02155-9.

59 I. P. Vali, B. S. Anusha, M. Pruthvija, S. Savitha, S. Ravindra, M. Nagaveni, P. S. Poojitha and N. Swathi, Bamboo and Coconut Shell Based Activated Carbon: A Raman Spectroscopic Study, *Mater. Chem. Phys.*, 2024, **318**, 129240, DOI: 10.1016/j.matchemphys.2024.129240.

60 M. A. Baqiya, A. Y. Nugraheni, W. Islamiyah, A. F. Kurniawan, M. M. Ramli, S. Yamaguchi, Y. Furukawa, S. Soontaranon, E. G. R. Putra, Y. Cahyono and D. Risdiana, Structural Study on Graphene-Based Particles Prepared from Old Coconut Shell by Acid–Assisted Mechanical Exfoliation, *Adv. Powder Technol.*, 2020, **31**(5), 2072–2078, DOI: 10.1016/j.apt.2020.02.039.

61 K. K. Ilavenil, P. Pandian and A. Kasthuri, Adsorption Study of Removal of Lead Ions Using Prosopis Juliflora and Prediction by Artificial Neural Network Modeling, *Mater. Today Proc.*, 2023, **72**, 2344–2350, DOI: 10.1016/j.matpr.2022.09.402.

62 P. Baghel and P. Kaushal, Rapid Synthesis of Carbon Nanotubes from Prosopis Juliflora Biochar Using Microwave Irradiation, *Mater. Sci. Eng., B*, 2022, **286**, 115987, DOI: 10.1016/j.mseb.2022.115987.

63 M. Thommes, K. Kaneko, A. V. Neimark, J. P. Olivier, F. Rodriguez-Reinoso, J. Rouquerol and K. S. W. Sing, Physisorption of Gases, with Special Reference to the Evaluation of Surface Area and Pore Size Distribution (IUPAC Technical Report), *Pure Appl. Chem.*, 2015, **87**(9–10), 1051–1069, DOI: 10.1515/pac-2014-1117.

64 V. Khorram Abadi, D. Habibi, S. Heydari and M. Ariannezhad, The Effective Removal of Ni^{2+}, Cd^{2+}, and Pb^{2+} from Aqueous Solution by Adenine-Based Nano-Adsorbent, *RSC Adv.*, 2023, **13**(9), 5970–5982, DOI: 10.1039/D2RA07230K.

65 H. S. Abu Salem, S. S. Hassan, F. A. Refay, Z. K. Sulieman, M. Y. Mohamed, A. R. Rabea, N. S. Refaay, S. Y. Abdel Moain, M. E.-S. Abdulrahman, O. N. Radwan, M. A. Roshdy and F. M. Mohamed, Modified Bentonite @ Microwave for Mn(VII) Removal with a Simulation Study, *Sci. Rep.*, 2025, **15**(1), 8520, DOI: 10.1038/s41598-025-91906-z.

66 Y. Pang, C. Zhao, Y. Li, Q. Li, X. Bayongzhong, D. Peng and T. Huang, Cadmium Adsorption Performance and Mechanism from Aqueous Solution Using Red Mud Modified with Amorphous MnO2, *Sci. Rep.*, 2022, **12**(1), 4424, DOI: 10.1038/s41598-022-08451-2.

67 Y. Chen, J. Yang and A. Abbas, Enhanced Chromium (VI) Adsorption onto Waste Pomegranate-Peel-Derived Biochar for Wastewater Treatment: Performance and Mechanism, *Toxics*, 2023, **11**(5), 440, DOI: 10.3390/toxics11050440.

68 H. Yazid, T. Bouzid, E. m. El mouchtari, L. Bahsis, M. El Himri, S. Rafqah and M. El haddad, Insights into the Adsorption of Cr(VI) on Activated Carbon Prepared from Walnut Shells: Combining Response Surface Methodology with Computational Calculation, *Clean Technol.*, 2024, **6**(1), 199–220, DOI: 10.3390/cleantechnol6010012.

69 D. Jia, Z. Jing, Y. Duan and J. Li, Ultrafast Removal of Cr(VI) Ions Using Polyamine Modified Carbon Nanotubes, *J. Taiwan Inst. Chem. Eng.*, 2022, **133**, 104265, DOI: 10.1016/j.jtice.2022.104265.

70 L. A. Malik, A. H. Pandith, A. Qureashi, A. Bashir and T. Manzoor, The Emerging Role of Quantum Computations in Elucidating Adsorption Mechanism of

Heavy Metal Ions: A Review, *Chem. Pap.*, 2022, **76**(6), 3351–3370, DOI: 10.1007/s11696-022-02106-2.

71 A. H. Romero, D. C. Allan, B. Amadon, G. Antonius, T. Applencourt, L. Baguet, J. Bieder, F. Bottin, J. Bouchet, E. Bousquet, F. Bruneval, G. Brunin, D. Caliste, M. Côté, J. Denier, C. Dreyer, P. Ghosez, M. Giantomassi, Y. Gillet, O. Gingras, D. R. Hamann, G. Hautier, F. Jollet, G. Jomard, A. Martin, H. P. C. Miranda, F. Naccarato, G. Petretto, N. A. Pike, V. Planes, S. Prokhorenko, T. Rangel, F. Ricci, G.-M. Rignanese, M. Royo, M. Stengel, M. Torrent, M. J. van Setten, B. Van Troeye, M. J. Verstraete, J. Wiktor, J. W. Zwanziger and X. Gonze, ABINIT: Overview and Focus on Selected Capabilities, *J. Chem. Phys.*, 2020, **152**(12), 124102, DOI: 10.1063/1.5144261.

72 M. J. Frisch, G. W. Trucks, H. B. Schlegel, G. E. Scuseria, M. A. Robb, J. R. Cheeseman, G. Scalmani, V. Barone, G. A. Petersson, H. Nakatsuji, X. Li, M. Caricato, A. V. Marenich, J. Bloino, B. G. Janesko, R. Gomperts, B. Mennucci, H. P. Hratchian, J. V. Ortiz, A. F. Izmaylov, J. L. Sonnenberg, D. Williams-Young, F. Ding, F. Lipparini, F. Egidi, J. Goings, B. Peng, A. Petrone, T. Henderson, D. Ranasinghe, V. G. Zakrzewski, J. Gao, N. Rega, G. Zheng, W. Liang, M. Hada, M. Ehara, K. Toyota, R. Fukuda, J. Hasegawa, M. Ishida, T. Nakajima, Y. Honda, O. Kitao, H. Nakai, T. Vreven, K. Throssell, J. A. Montgomery Jr, J. E. Peralta, F. Ogliaro, M. J. Bearpark, J. J. Heyd, E. N. Brothers, K. N. Kudin, V. N. Staroverov, T. A. Keith, R. Kobayashi, J. Normand, K. Raghavachari, A. P. Rendell, J. C. Burant, S. S. Iyengar, J. Tomasi, M. Cossi, J. M. Millam, M. Klene, C. Adamo, R. Cammi, J. W. Ochterski, R. L. Martin, K. Morokuma, O. Farkas, J. B. Foresman, and D. J. Fox, *Gaussian 16 Revision C.01*, Gaussian Inc., Wallingford, CT, 2016.

73 E. Flórez, C. Jimenez-Orozco and N. Acelas, Unravelling the Influence of Surface Functional Groups and Surface Charge on Heavy Metal Adsorption onto Carbonaceous Materials: An in-Depth DFT Study, *Mater. Today Commun.*, 2024, **39**, 108647, DOI: 10.1016/j.mtcomm.2024.108647.

74 S. F. Sousa, P. A. Fernandes and M. J. Ramos, General Performance of Density Functionals, *J. Phys. Chem. A*, 2007, **111**(42), 10439–10452, DOI: 10.1021/jp0734474.

75 P. J. Hay and W. R. Wadt, Ab Initio Effective Core Potentials for Molecular Calculations. Potentials for the Transition Metal Atoms Sc to Hg, *J. Chem. Phys.*, 1985, **82**(1), 270–283, DOI: 10.1063/1.448799.

76 R. Dennington, T. A. Keith, and J. M. Millam, *GaussView, Version 6.0.16*, Semichem Inc., Shawnee Mission, KS, 2016.

77 M. Khnifira, W. Boumya, J. Attarki, A. Mahsoune, M. Sadiq, M. Abdennouri, S. Kaya and N. Barka, A Combined DFT, Monte Carlo, and MD Simulations of Adsorption Study of Heavy Metals on the Carbon Graphite (111) Surface, *Chem. Phys. Impact*, 2022, **5**, 100121, DOI: 10.1016/j.chphi.2022.100121.

78 E. J. C. M. Gomes, V. S. Macedo, A. K. dos Santos Pereira, G. S. Cavallini and D. H. Pereira, Theoretical Study of the Adsorption Capacity of Potentially Toxic Cd2+, Pb2+, and Hg2+ Ions in Hemicellulose Matrices, *Int. J. Biol. Macromol.*, 2024, **258**, 128894, DOI: 10.1016/j.ijbiomac.2023.128894.

79 T. Koopmans, Über Die Zuordnung von Wellenfunktionen Und Eigenwerten Zu Den Einzelnen Elektronen Eines Atoms, *Physica*, 1934, **1**(1–6), 104–113, DOI: 10.1016/S0031-8914(34)90011-2.

80 R. F. W. Bader and H. Essén, The Characterization of Atomic Interactions, *J. Chem. Phys.*, 1984, **80**(5), 1943–1960, DOI: 10.1063/1.446956.

81 R. F. W. Bader, *Atoms in Molecules: A Quantum Theory*, Oxford University Press, Oxford, 1994.

82 D. Khalla, K. Belguidoum, M. Nacef, M. Boukour, M. L. Chelaghmia, O. Khelifi, R. Selaimia, N. Bengourna, A. M. Affoune and H. Amira-Guebailia, Competitive Adsorption of Quinary Heavy Metal Ions onto Chestnut Shell Activated Carbon, *Mater. Chem. Phys.*, 2024, **323**, 129646, DOI: 10.1016/j.matchemphys.2024.129646.

83 D. T. Reis, I. H. S. Ribeiro and D. H. Pereira, DFT Study of the Application of Polymers Cellulose and Cellulose Acetate for Adsorption of Metal Ions (Cd2+, Cu2+ and Cr3+) Potentially Toxic, *Polym. Bull.*, 2020, **77**(7), 3443–3456, DOI: 10.1007/s00289-019-02926-5.